

## Chapter 2

# Raman Imaging in Semiconductor Physics: Applications to Microelectronic Materials and Devices

Antoine Tiberj and Jean Camassel

**Abstract** The unique versatility of micro-Raman spectroscopy ( $\mu$ RS) in semiconductor physics remains in Raman imaging. Numerous applications cover the whole development of modern electronic and optoelectronic devices: from semiconductor growth to advanced device inspection tools. In this chapter, a wide variety of semiconductors (SiC, graphene, GaN, GaAs, SiGe, strained Si, sSOI, SGOI) and devices (FETs, lasers, MEMS) are addressed. First, it will be shown how Raman mapping enables to check the crystalline quality, the composition, the doping, and the uniformity of as-grown semiconductors. Then, we will focus on the most popular application in microelectronics: strain measurements either at the device or at the full wafer scale. Finally, we will show how  $\mu$ RS imaging can be used for final device inspection through the temperature mapping of operating devices (FETs, lasers, actuators).

Since the first report by Raman in 1928 [1, 2], Raman spectroscopy has become increasingly popular in materials science and, especially, in semiconductor physics and microelectronics. Basically Raman scattering probes the inelastic scattering of a monochromatic light (incoming-photons) by the atomic vibrations in a medium (solid, liquid, or gas). In crystalline solids, the atomic vibrations are quantized (phonons) and they are very sensitive to internal and external perturbations, such as doping and stress. The frequency of the scattered light (out-coming photons) is then a local probe of the perturbation experienced (or not) by the medium.

Today, the large number of results collected on semiconductors, combined with a good theoretical understanding of the scattering mechanisms, allows to predict reli-

---

A. Tiberj (✉) · J. Camassel  
Laboratoire Charles Coulomb UMR 5221, Université Montpellier 2,  
34095 Montpellier, France  
e-mail: Antoine.Tiberj@univ-montp2.fr

A. Tiberj · J. Camassel  
Laboratoire Charles Coulomb UMR 5221, CNRS,  
34095 Montpellier, France  
e-mail: Jean.Camassel@univ-montp2.fr

ably the effect of an external perturbation on the electronic and vibrational properties of the investigated medium (either ordered or disordered). Raman spectroscopy can then be used to identify the constituting species, study the compositional uniformity, crystallinity, doping level, and to probe locally the temperature and stress.

At the industrial level, in modern clean room facilities micro-Raman spectroscopy ( $\mu$ RS) has become (like many other optical techniques) a very attractive characterization tool. This is because of its contactless and nondestructive nature. Thanks to recent turnkey Raman systems, one can perform repetitively large area mapping with spatial resolution down to 300 nm. The use of several laser wavelengths enables then to probe the in-depth profile of a given semiconductor or device. All these features confirm the unique versatility and potentialities of  $\mu$ RS imaging in microelectronics.

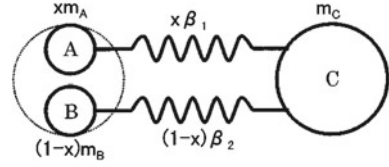
In this chapter, we illustrate how this unique characterization tool covers the whole process flow of fabrication of modern electronic and optoelectronic devices. The first section will give some background considerations on Raman imaging in semiconductor physics. The second section will be devoted to the study of advanced wafers manufacturing and epitaxial layers development, such as graphene,  $\text{Si}_{1-x}\text{Ge}_x$  alloys, and strained Si wafers. The third section will focus on the most popular application of Raman imaging in microelectronics: stress monitoring. Finally the fourth one will address how Raman imaging can contribute to the final device inspection.

## 2.1 Background Considerations

In this section, we remind briefly the basic principles of Raman scattering in a semiconductor. We limit ourselves to first-order Raman scattering because higher order processes are seldom used for Raman imaging purpose. For a more detailed introduction and description of  $\mu$ RS in materials science, and especially in semiconductors, please refer to [3–5]. For a general review of  $\mu$ RS in nanomaterials, including SiC optical fibers for telecommunications, see [6].

First-order Raman scattering is nothing but a two-photon event that involves the simultaneous annihilation of an incident photon and the creation of a scattered photon. Consider, for instance, a monochromatic light beam of frequency  $\nu_i$  reaching a crystal. Most of the incident photons will be either reflected or transmitted or absorbed following the standard laws of reflection and transmission. Among the last part, some will be elastically (Rayleigh) scattered. The remaining ones will be inelastically scattered by the emission (or absorption) of a phonon having a frequency  $\nu_p$ . The emission of a phonon corresponds to the Stokes process. The absorption corresponds to the anti-Stokes process. In both cases, this inelastic scattering must satisfy the conservation of energy and momentum. This means that the scattered photons have a frequency  $\nu_s = \nu_i \pm \nu_p$ . Wave vector conservation means also that the first-order spectra display only a discrete set of peaks, corresponding to phonon energy values at the center of the Brillouin zone. Usually, the linewidth is very sharp and any (weak) perturbation induced by a structural change, by fluctuations of the composition, the doping level or a local strain can be easily detected.

**Fig. 2.1** Pseudo-unit-cell of a ternary alloy of the form  $A_xB_{1-x}C$ . The effective masses are respectively  $xm_A$ ,  $(1-x)m_B$  and  $m_C$ . The corresponding force constants are  $x\beta_1$  and  $(1-x)\beta_2$  [7]



### 2.1.1 Compositional Changes

Compositional changes are important parameters in the case of opto-electronic devices (like IR detectors for instance) in which the active part is made of a ternary or quaternary alloy in order to tune the optical response. In such systems, the simplest approach is to define a pseudo-unit cell (PUC) such that for a ternary alloy of the form  $A_xB_{1-x}C$ , for instance, all atoms C are surrounded by A and B atoms with effective mass  $xm_A$  and  $(1-x)m_B$ , respectively [7]. This is shown in Fig. 2.1. The corresponding force constants are  $x\beta_1$  and  $(1-x)\beta_2$  and the composition dependence of phonon frequencies can be obtained from a simple  $2 \times 2$  matrix like:

$$\begin{vmatrix} b_{11} + m_{11}\omega^2 & b_{12} + m_{12}\omega^2 \\ b_{21} + m_{21}\omega^2 & b_{22} + m_{22}\omega^2 \end{vmatrix} = 0 \quad (2.1)$$

Since Eq. 2.1 is a quadratic equation, there are always two solutions for a given composition  $x$ . The usual classification in terms of one-mode, two-modes or mixed modes behavior comes from the consideration of the different coupling coefficients with the incoming light.

In group IV binary alloys, like  $\text{Si}_{1-x}\text{Ge}_x$  for instance, the situation appears more complicated. Any substitutional atom can sit on any of the two sublattices and, in both cases, there is a strong local distortion that accompanies the substitution. In such a case, both strain and alloying must be simultaneously taken into account. To this end, R  cker and Methfessel have developed an anharmonic Keating model [8] that predicts for the Si-Si Raman mode on the  $\{001\}$  face of  $\text{Si}_{1-x}\text{Ge}_x$  [9]:

$$\Delta\omega_{\text{Si-Si}} = -69x - 780\varepsilon \quad (2.2)$$

which is in excellent agreement with the experimental results summarized in Ref. [10]:

$$\Delta\omega_{\text{Si-Si}} = -68x - 830\varepsilon \quad (2.3)$$

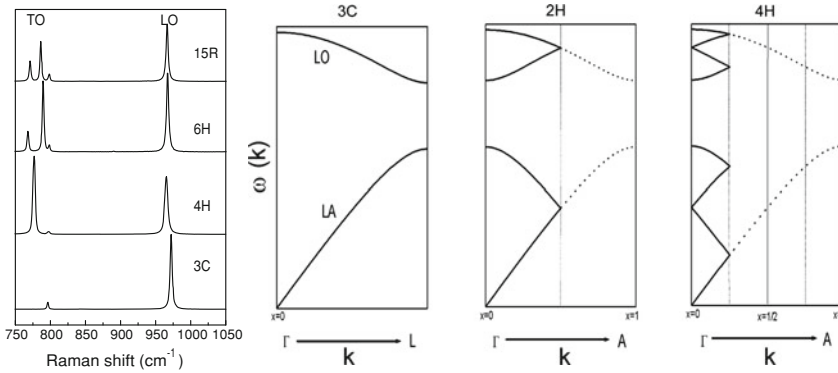


**Fig. 2.2** Raman spectra of the most common SiC polytypes (3C, 4H, 6H, 15R). Their increased complex Raman fingerprint allows an easy polytype identification and can be used to image polytype inclusion in SiC substrates. Dispersion curves for the 3C, 2H, 4H polytypes. The increased complexity comes from the folding of the (3C) unit cell as the length of the unit cell increases along the  $c$  axis

### 2.1.2 Change in Crystal Structure

Structural changes are seldom observed in III–V alloys but may appear in some cases, as the composition reaches  $x = 0.5$ . This is, for instance, the triclinic (Cu–Pt like) form of  $\text{GaInP}_2$ . Structural changes also appear in binary compounds, like GaN or SiC, as the total energy difference between two crystallographic structures is small. This is the case of the cubic and wurtzite forms of GaN. This is also the case of the numerous polytypes of SiC [5, 11].

As a matter of fact, SiC exhibits a very large number of polytypes (250) with different structural and physical properties. All polytypes have the same chemical composition but presents different crystallographic structures (cubic, hexagonal, rhombohedral) that differ only by the stacking sequence of  $N$  elemental Si–C bilayers in the unit cell. For a review see [12]. The most investigated (crystalline) forms are 4H, 6H, and 3C–SiC. Among them, 4H–SiC has long been recognized for a large variety of high-power and high-temperature electronic applications. 6H–SiC is more considered as substrate for the growth of graphene or nitride semiconductors. 3C–SiC could replace both of them but suffers from the lack of substrate. In polycrystalline form, SiC nanowires have demonstrated interest for field emission devices [13] while SiC fibres have been used to strengthen nano-composite materials [6].

Whatever the application, one of the main concern for SiC wafers manufacturers is to check the absence of polytype inclusion, the crystalline quality [14] and the doping uniformity [15]. Figure 2.2 shows an illustration of the first application. On the left panel, we display four different Raman spectra which appear for the 3C, 4H, 6H and 15R polytypes, with increasingly complex Raman fingerprints. This comes from the folding of the cubic (3C) unit cell as the length of the unit cell increases along the  $c$  axis (right panel).

### 2.1.3 Doping and Doping Uniformity

Raman imaging can be used to measure the doping level and, even more important, the doping uniformity in polar semiconductors. This spatial homogeneity is a crucial point since inhomogeneous doping often impacts the thermal process steps used to manufacture the devices and degrades their performances.

The carrier concentration measurements are based on the strong influence of the phonon–plasmon coupling on the Raman shift and lineshape of the longitudinal optical phonons in polar media. As the carrier’s density increases, the LO phonon mode shifts to higher frequency and broadens asymmetrically. This is because the carrier’s collective modes of oscillations (called plasmons) modify the dielectric constant. The macroscopic electric field associated with the plasmons interacts with the longitudinal optical phonons. This interaction modifies the Raman cross-sections and this leads to coupled modes of mixed phonon–plasmon character (LPP mode) as the plasmon frequency approaches the phonon ones. The Raman shape of this mode is more and more distorted. In SiC [16] or GaN [17], it occurs for concentrations of technological interests in the  $10^{17}$ – $10^{19}$  cm $^{-3}$  range.

The lineshape of a LPP mode can be simply modeled using [16]:

$$I(\omega) = SA(\omega) \operatorname{Im} \left( \frac{-1}{\epsilon(\omega)} \right) \quad (2.4)$$

where

$$A(\omega) = 1 + \frac{2C\omega_{\text{TO}}^2 \left[ \omega_p^2 \gamma (\omega_{\text{TO}}^2 - \omega^2) - \omega^2 \Gamma (\omega^2 - \gamma^2 - \omega_p^2) \right]}{\Delta} \\ + \frac{C^2 \omega_{\text{TO}}^4 \left\{ \omega_p^2 \left[ \gamma (\omega_{\text{LO}}^2 - \omega_{\text{TO}}^2) + \Gamma (\omega_p^2 - 2\omega^2) \right] + \omega^2 \Gamma (\omega^2 + \gamma^2) \right\}}{\Delta (\omega_{\text{LO}}^2 - \omega_{\text{TO}}^2)} \quad (2.5)$$

and

$$\Delta = \omega_p^2 \gamma \left[ (\omega_{\text{TO}}^2 - \omega^2)^2 + (\omega \Gamma)^2 \right] + \omega^2 \Gamma (\omega_{\text{LO}}^2 - \omega_{\text{TO}}^2) (\omega^2 + \gamma^2) \quad (2.6)$$

$\omega_{\text{LO}}$  and  $\omega_{\text{TO}}$  are the longitudinal and transverse optical phonon frequencies,  $\gamma$  is the plasmon dampening constant which is related to the carrier’s mobility,  $\Gamma$  is the phonon dampening constant, and  $C$  is the Faust-Henry coefficient.  $S$  is a proportionality factor. For 4H-SiC, the following values are commonly used:  $\omega_{\text{TO}} = 783$  cm $^{-1}$ ,  $\omega_{\text{LO}} = 965$  cm $^{-1}$ , and  $C = 0.43$ .

The dielectric function  $\epsilon(\omega)$  in Eq. 2.4 can be written as the sum of a phonon and a plasmon contribution:

$$\epsilon(\omega) = \epsilon_{\infty} \left( 1 + \frac{\omega_{\text{LO}}^2 - \omega_{\text{TO}}^2}{\omega_{\text{TO}}^2 - \omega^2 - i\omega\Gamma} - \frac{\omega_p^2}{\omega(\omega + i\gamma)} \right) \quad (2.7)$$

where  $\omega_p$  is the plasmon frequency. For carriers in a single, isotropic and parabolic band the plasmon frequency is given by:

$$\omega_p^2 = \frac{ne^2}{m^*\epsilon_{\infty}} \quad (2.8)$$

where  $n$  is the carrier concentration,  $m^*$  their effective mass, and  $\epsilon_{\infty}$  the high-frequency dielectric function.

### 2.1.4 Strain

All semiconductor devices are subjected to strain or stress. The stress can be internal (residual stress) or external (applied stress) but, in any case, the associated strain changes the equilibrium position of the atoms in the lattice. This alters the phonon properties due to the anharmonic components of the interatomic potential and the phonon frequencies corresponding to the deformed crystal are shifted. The shifts are of the order of 0.1 % of the mode frequency and can be calculated as a perturbative effect [18].

For a cubic crystal like Si, the new phonon frequencies and polarization vectors will be given respectively by the eigenvalues and eigenvectors of the secular equation [19]:

$$\begin{vmatrix} p\epsilon_{xx} + q(\epsilon_{yy} + \epsilon_{zz}) - \lambda & 2r\epsilon_{xy} & 2r\epsilon_{xz} \\ 2r\epsilon_{xy} & p\epsilon_{yy} + q(\epsilon_{xx} + \epsilon_{zz}) - \lambda & 2r\epsilon_{yz} \\ 2r\epsilon_{xz} & 2r\epsilon_{yz} & p\epsilon_{zz} + q(\epsilon_{xx} + \epsilon_{yy}) - \lambda \end{vmatrix} = 0 \quad (2.9)$$

with  $\lambda = \omega^2 - \omega_0^2$ . For small values of strain, this can be simplified and gives:

$$\Delta\omega = \omega - \omega_0 \sim \frac{\lambda}{2\omega_0} \quad (2.10)$$

$p$ ,  $q$ ,  $r$  are the so-called phonon deformation potentials which are related to the changes in the spring constant due to the strain,  $\omega_0$  is the frequency of the triply degenerated phonon and  $\omega$  is the new frequency of the phonon for the strained crystal. The reference axes  $x$ ,  $y$  and  $z$  correspond to [100], [010], and [001], respectively. To deduce from the selection rules, which phonon mode can be observed, the experimental scattering configuration must be taken into account. The intensity of a given Raman mode is then given by:

$$I \propto \sum_j |\mathbf{e}_i \cdot \mathbf{R}_j \cdot \mathbf{e}_s|^2 \quad (2.11)$$

where  $\mathbf{e}_i$  and  $\mathbf{e}_s$  are the polarization vectors of the incident and scattered light while  $\mathbf{R}_j$  are Raman tensors. For a cubic crystal like Si, they are given (in the absence of stress) by:

$$\mathbf{R}_x = \begin{pmatrix} 0 & 0 & 0 \\ 0 & 0 & d \\ 0 & d & 0 \end{pmatrix} \quad \mathbf{R}_y = \begin{pmatrix} 0 & 0 & d \\ 0 & 0 & 0 \\ d & 0 & 0 \end{pmatrix} \quad \mathbf{R}_z = \begin{pmatrix} 0 & d & 0 \\ d & 0 & 0 \\ 0 & 0 & 0 \end{pmatrix} \quad (2.12)$$

As an example, let us consider strained silicon grown on top a relaxed SiGe layer. It is subjected to a biaxial tensile stress in the  $x$ - $y$  plane, with stress components  $\sigma_{xx} = \sigma_{yy} = \sigma$ . The corresponding strain components are given by the Hooke's law:

$$\begin{aligned} \varepsilon_{xx} &= \varepsilon_{yy} = (S_{11} + S_{12})\sigma \\ \varepsilon_{zz} &= 2S_{12}\sigma \\ \varepsilon_{xy} &= \varepsilon_{xz} = \varepsilon_{yz} = 0 \end{aligned} \quad (2.13)$$

Solving the (diagonal) secular equation 2.9 then gives:

$$\begin{aligned} \Delta\omega_x &= \Delta\omega_y = \frac{(p+q)S_{11} + (p+3q)S_{12}}{2\omega_0} \sigma \\ \Delta\omega_z &= \frac{qS_{11} + (p+q)S_{12}}{\omega_0} \sigma \end{aligned} \quad (2.14)$$

Clearly, in this simple case, the phonon polarizations and the Raman tensors  $\mathbf{R}_j$  remain unchanged. Moreover, from backscattering from a {001} surface, only the phonon frequency  $\omega_z$  can be probed. Using the numerical values given in Table 2.1 yields then a numerical relationship between the stress, the strain and the Raman shift:

$$\Delta\omega_z (\text{cm}^{-1}) = -4.6\sigma (\text{GPa}) = -830\varepsilon_{xx} \quad (2.15)$$

In a more general case, given a stress (or strain) tensor and an experimental configuration, one can (easily) deduce the relationship between the Raman frequency shifts and the strain level. Unfortunately, performing the reciprocal is quite impossible. Six independent Raman data are needed to determine exactly the strain tensor without any assumptions. These six data are the frequency shifts and intensities of the three Raman modes which can seldom be simultaneously measured and mapped at the  $\mu\text{RS}$  scale. To obtain a quantitative estimation of the strain, one has to presuppose a strain model or to compare the experimental with the strain calculated from finite-element modeling [20–23].

**Table 2.1** Phonon deformation potentials and elastic constants of silicon [24] and diamond [25]

	$p/\omega_0^2$	$q/\omega_0^2$	$r/\omega_0^2$	$S_{11}$ (GPa <sup>-1</sup> )	$S_{12}$ (GPa <sup>-1</sup> )	$S_{44}$ (GPa <sup>-1</sup> )
Silicon	-1.85	-2.31	-0.71	$7.69 \times 10^{-3}$	$-2.14 \times 10^{-3}$	$12.6 \times 10^{-3}$
Diamond	-2.81	-1.77	-1.9	$0.952 \times 10^{-3}$	$-0.099 \times 10^{-3}$	$1.737 \times 10^{-3}$

## 2.2 Application to Advanced Wafers Manufacturing and Epitaxial Layers Development

In the literature, Raman imaging has often been used to check the uniformity of wafers or epitaxial layers such as InN [26] or graphene [27]. Investigations of the strain present in conformal GaAs grown on Si wafers [28] or GaN/AlN multilayers grown on a mesh-patterned Si(111) substrate [29, 30] have also been reported. In this section, we will focus on three different examples: the development of SiC wafers for power device applications, the growth of graphene on SiC (one of the most exciting material system today) and, finally, the development of strained-silicon layers to increase the channel mobility in C-MOS technology.

### 2.2.1 Development of 4H-SiC Wafers

In the recent years, much work has been done in this field. Focusing on a few typical examples: in Japan, Nakashima et al. studied modulation-doped 6H-SiC crystals by Raman imaging [31] and extracted from the Raman spectra the carrier's density and mobility profiles of the as-grown crystals; in Europe, more emphasize was made on the parallel development of *n*-type and *p*-type SiC wafers. This is shown in Fig. 2.3 which displays two different series of spectra collected on 2 in 4H-SiC wafers [14, 15]. From top to bottom are:

1. A series of experimental spectra fitted with the model of Sect. 2.1.3. Standard fitting procedures enable to determine the plasmon frequency  $\omega_p$  and its dampening constant  $\gamma$ . The carrier's density and mobility can then be extracted [31]. This extraction can be simplified by calibrating the shift and/or broadening of the LO phonon with the doping [14] or by considering only the high frequency coupled plasmon-phonon mode in the limit of no dampening. However, the latter technique tends to slightly underestimate the carrier's density. This can be seen in Fig. 6 of Ref. [15].
2. Application of this procedure to determine the doping profile across two 4H-SiC wafers is shown in Fig. 2.3b. Measuring along the diameter of 2 in wafers, the shift of the LO phonon gives an estimate of the nitrogen concentration which is plotted in Fig. 2.3b. The spatial dependence varies from one wafer to another and is not symmetric with respect to rotations of the wafer. Moreover, the doping level at the edges is much lower than the nominal nitrogen concentration noted



in the legend. These results were compared to resistivity maps performed on the same wafers. The maps confirmed the high nonuniformity of doping and were in good agreement with the Raman data.

3. For comparison, in Fig. 2.3c, d two examples of data collected on *p*-type wafers are shown [14]. The strain field surrounding two screw dislocations is imaged in Fig. 2.3c by measuring the strain-induced frequency shift of the  $E_2(\text{TO})$  mode. Optical microscopy evidenced that these screw dislocations are associated with two micropipes, which are device killers for SiC electronics. The Raman map of the LO phonon broadening (Fig. 2.3d) performed in the same area exhibits a sixfold symmetry along the crystallographic  $\langle 1\text{-}210 \rangle$  directions in the hexagonal SiC lattice. This LO phonon broadening was attributed to a variation of the carrier's density due to a dopant depletion/accumulation in the vicinity of the dislocation network induced by the micropipes.

### 2.2.2 Graphene Growth on SiC

To date, among the emerging research materials, graphene has been identified as a promising candidate to complement silicon in forthcoming generations of high frequency circuits [32]. As a matter of fact, graphene has outstanding electronic, optical, thermal, and mechanical properties [33–35] and, recently, Geim and Novoselov shared the 2010 Nobel Prize in Physics for groundbreaking experiments [36].

Graphene is nothing but a single sheet of carbon atoms packed in a honeycomb lattice in which strong  $sp^2$  covalent bonds are formed. Excepting diamond, it constitutes the 2D building block of all carbon allotropes. It can be wrapped into 0D fullerenes, rolled into 1D carbon nanotubes, or stacked into 3D graphite [37]. Most of the electronic properties of graphene (including mass-less Dirac fermions, high carriers mobility, and ballistic transport properties at room temperature) come from its linear band structure with 6 double cones at the inequivalent K and K' points of the Brillouin zone. This linear dispersion was predicted a long time ago by Wallace in 1947 [38] and gives rise to an unusual quantum Hall effect [39, 40] that remains at room temperature [41]. Graphene can then be used to develop new resistance standard for metrology applications [42]. It is also transparent, stronger than steel, and also has a very high thermal conductivity. Therefore, a wide range of potential applications has been identified like: flexible electronics, gas sensors, transparent conductor for touch screens, liquid crystal displays, photovoltaic cells, and organic light-emitting diodes.

However, and because of the so-called Kohn anomaly (which is nothing but the failure of the usual adiabatic Born–Oppenheimer approximation in zero-gap semiconductors [43]) it is also a perfect example to illustrate all the applications of  $\mu\text{RS}$  that have been mentioned before. Raman spectroscopy on few layers graphene (FLG) can not only evaluate the crystalline quality but also the thickness, the stacking order of graphene sheets, the doping level and, finally, the residual strain.

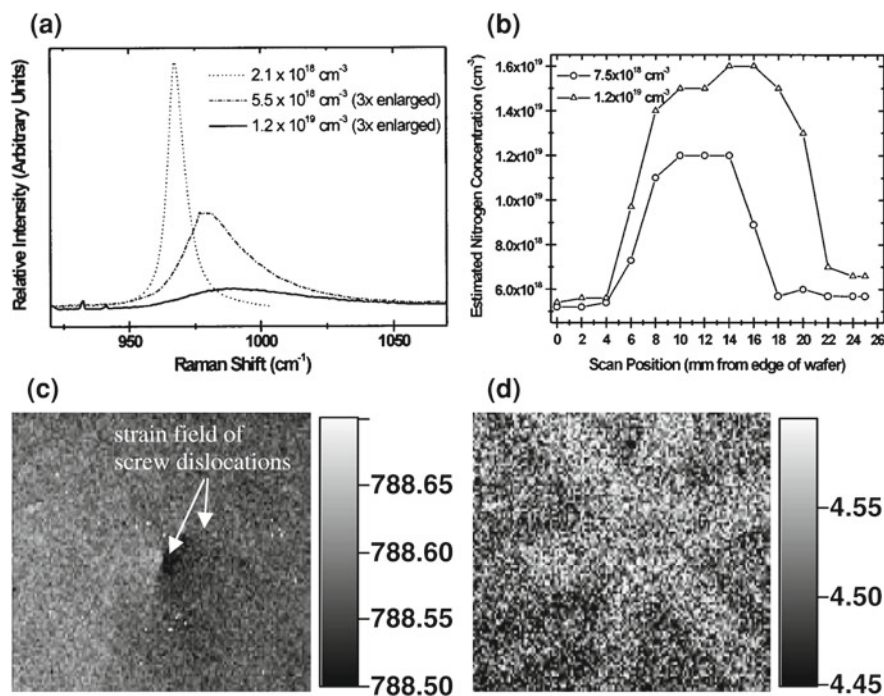


**Fig. 2.3** **a** Influence of carrier's density on the Raman spectrum of the SiC A<sub>1</sub> LO phonon mode. As the carrier's density is increased from  $2.1 \times 10^{18}$  to  $1.2 \times 10^{19} \text{ cm}^{-3}$ , the A<sub>1</sub> LO phonon shifts to higher frequency and asymmetrically broadens; **b** Raman imaging can then be applied to evaluate the profile of the nitrogen concentration across the diameter of 2 4H-SiC wafers. The nominal doping levels are indicated in the legend. Reprinted with permission from [15]. Copyright 1998, American Institute of Physics; **c** micro-Raman map of the strain-induced frequency shift of the E<sub>2</sub> TO mode around two screw dislocations. These dislocations are associated with the presence of two micropipes which are surrounded by a dislocation network having a sixfold symmetry [14]; **d** micro-Raman map of the LO phonon broadening which can be explained by an acceptor accumulation/depletion around this dislocation network. These doping fluctuations shows clearly the sixfold symmetry of this dislocation network. Reprinted from [14]. Copyright 2005, with permission from Wiley-VCH

To date, graphene has been produced using many different ways:

1. Mechanical exfoliation of graphite using scotch tape [37].
2. Chemical exfoliation using either redox reaction [44] or solvent [45].
3. Chemical vapor deposition (CVD) on metal surfaces such as Ru [46], Ir [47, 48], Ni [49–51], and Cu [52, 53].
4. High-temperature annealing ( $> 1,100^\circ\text{C}$ ) of a SiC surface [54, 55].

The last technique is one of the most promising method to get large-scale graphene wafers of high quality and uniformity. It consists in a controlled sublimation of few Si atomic layers from a single crystalline SiC surface [54–60]. During the sublimation, the remaining C atoms rearrange themselves and form FLG which are called

“epitaxial graphene” (EG) layers. Such EG samples can be grown either on the Si face (0001) of a SiC substrate or on the C face (000 $\bar{1}$ ). The main differences between EG grown on the C and the Si face come from the SiC surface reconstruction and its interaction with the first graphene sheet.

On the Si face, the graphene planes are Bernal (AB) stacked on top of a  $6\sqrt{3} \times \sqrt{3}R30$  SiC surface with a so-called “buffer layer” in between. This “buffer layer” is composed of an intermediate C-rich layer with remaining covalent bonds with Si atoms of the SiC surface [59–61]. As a consequence, EG on the Si-face is (usually) highly *n*-type doped (around  $10^{13} \text{ cm}^{-2}$ ) with a low carrier mobility (few thousands  $\text{cm}^2 \text{ V}^{-1} \text{ s}^{-1}$ ).

On the C-face the situation is completely different. There is no need for a “buffer layer” anymore but two different pristine surface reconstructions have been evidenced below the graphene layers:  $(2 \times 2)_\text{C}$  and  $(3 \times 3)$  SiC surface reconstructions. The graphene layers may have several orientations on top of these surface reconstructions [62–64] and the stacking order can be either Bernal or turbostratic-like. Because of these different surface reconstructions, the interaction between the graphene layers and the C-face of SiC substrate is reduced compared to the one existing on the Si-face. Moreover, graphene grown on a  $(3 \times 3)$  SiC surface experiences the weakest interaction with the underlying substrate. This weaker interaction may be one of the reasons for the better carrier mobility measured on EG on the C-face ( $27,000 \text{ cm}^2 \text{ V}^{-1} \text{ s}^{-1}$ ) [54].

In this section, we review some recent Raman imaging results collected on EG grown on the C and Si-faces of 6H-SiC substrates [65, 66]. First, we briefly describe the growth techniques and the experimental set-up used for micro-Raman and micro-transmission imaging. Then, we discuss results collected on self-organized graphene ribbons grown on the C-face of 6H-SiC substrates and we show how the thicknesses, stacking order, and a rough estimate of the doping level can be obtained. Finally, FLG grown on the Si-face are investigated and we show how the compressive stress experienced by such FLGs can be estimated.

## Growth Technology

In this section, we will only consider samples grown using the processes described in [27, 65, 66], with a graphite cap to increase the C and Si partial pressures over the SiC surface. Such a graphite coverage lowers the Si out-diffusion rate during the growth and enables to perform FLG growth at higher temperature. This promotes better SiC surface reconstruction and on the C face of 6H-SiC substrates after 15 min annealing at  $1,700^\circ\text{C}$  in a secondary vacuum, the growth of long (self-organized) graphene ribbons can be done [65]. These ribbons are  $5 \mu\text{m}$  wide and  $150 \mu\text{m}$  long and fully occupy a single terrace of the heavily reconstructed (step-bunched) SiC surface [27]. On the Si face, the temperature was slightly higher ( $1,750^\circ\text{C}$  for 20 min under argon). A full graphene coverage was obtained with a similar (pronounced) step-like morphology of the SiC substrate [66]. The average terrace width was again  $5 \mu\text{m}$  with a remarkable homogeneity of width and orientation over a scale of  $1 \text{ cm}^2$ .

## Micro-Raman and Micro-Transmission Spectroscopy

Raman spectra were collected at room temperature, using a Jobin-Yvon Horiba T64000 spectrometer operated in the confocal mode. The 514 nm line of an Ar-Kr ion laser was used for excitation. With a x100 microscope objective, the spot diameter was about  $\sim 1 \mu\text{m}$  with, typically, 1 mW power focussed on the sample. To combine micro-Raman spectroscopy with micro-transmission experiments, a low noise photodiode was inserted between the SiC substrate and the XYZ piezoelectric stage. For details, see [27]. In this way, it was possible to measure (at the same time and using the same laser beam as probe) the power transmitted through the sample and the associated micro-Raman spectrum. The true FLG's spectra were obtained by subtracting the SiC reference signal from the experimental results.

The graphene extinction was deduced from the following equation:

$$\eta = \frac{T_0 - T}{T_0} \quad (2.16)$$

in which  $T_0$  is the bare SiC transmittance value and  $T$  the modified one which epitaxial FLGs on top. From the work of Ref. [67], this can be expressed as:

$$T = \frac{4n}{\left|1 + n + \frac{N\sigma}{\epsilon_0 c}\right|^2} \text{ in which } \sigma = \frac{\pi e^2}{2h} \quad (2.17)$$

In this equation,  $n = 2.68$  is the SiC refractive index,  $N$  the number of graphene layers and  $\sigma$  the optical conductivity of a single (isolated) graphene sheet that was confirmed experimentally [34]. The relative (theoretical) extinction of a monolayer and a bilayer graphene on top of a SiC substrate is then 1.23 and 2.44 %, respectively.

## Raman Imaging of Isolated Graphene Ribbons Grown on the C-Face

In Fig. 2.4, we show the results of the analysis of a large ( $20 \times 100 \mu\text{m}^2$ ) map collected on two neighboring graphene ribbons. The step size was  $0.5 \mu\text{m}$  for the X direction and  $2 \mu\text{m}$  for the Y direction. Six individual maps are shown. The first one corresponds to the extinction values, the second one to the integrated intensity of the G band normalized to the HOPG peak. The third one gives the normalized integrated intensity of the 2D band, while the fourth and fifth ones give the shift of the G and 2D bands, respectively. Finally, the last one corresponds to the absolute value of the Fermi level computed from the previous results. Of course, because of the limited range of the XY piezostage ( $100 \times 100 \mu\text{m}^2$ ) the two ribbons could not be completely probed. However, a first point to be noticed is that, on both ribbons, no D band map could be given. This is shown in greater detail in Fig. 2.5a, b and demonstrates the excellent crystalline quality of these graphene samples.

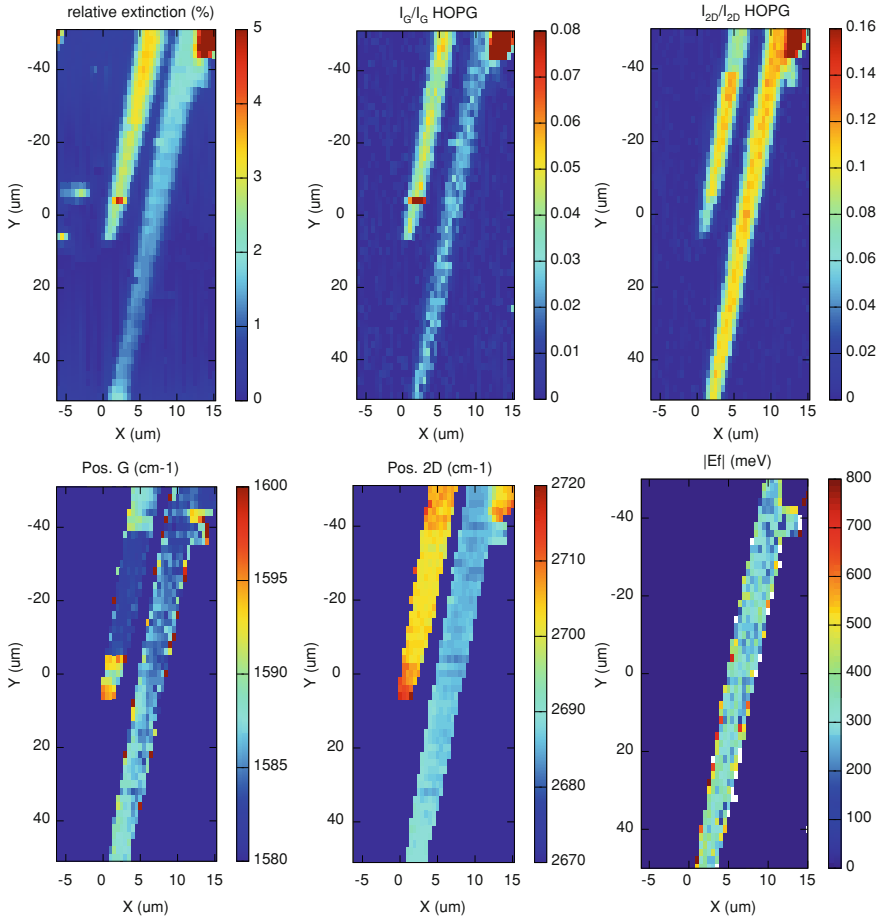


**Fig. 2.4**  $20 \times 100 \mu\text{m}^2$  maps of two graphene ribbons grown on the C-face of 6H-SiC. The step sizes are  $0.5$  and  $2 \mu\text{m}$  for the  $X$  and  $Y$  axes, respectively. The relative extinction, the normalized intensities, and Raman shifts of the G and 2D band are shown. The right left ribbon corresponds to a monolayer (bilayer) graphene. The absolute value of the Fermi level is evaluated from the ratio between the intensities of the 2D and G bands only for the monolayer. It corresponds to a doping level between  $3 \times 10^{12}$  and  $9 \times 10^{12} \text{ cm}^{-2}$  with an average of  $6 \times 10^{12} \text{ cm}^{-2}$

Let us now consider everything more in details. The first (extinction) map shows that both ribbons have an excellent thickness uniformity. However, and because the relative extinction is different, it shows also that the left one is thicker than the right one. Concerning the absolute values, from these extinction maps complemented by additional point by point measurements, we find that the thinner (right) ribbon corresponds with relative extinction values  $\eta$  ranging from  $1.2$  to  $1.4 \%$ . This shows that we deal with a true epitaxial monolayer graphene (MLG) ribbon. To ascertain this result, a Raman spectrum collected at the center of ribbon is shown in Fig. 2.5a (lower spectrum). It is clearly similar to the one reported in the literature [68] for

monolayers graphene exfoliated on top of an oxidized silicon substrate and all spectra collected on the same ribbon exhibited the same Raman fingerprint.

Typically, the G band falls between  $1,583$  and  $1,587 \text{ cm}^{-1}$ , with a FWHM of the order of  $13 \text{ cm}^{-1}$ , while the 2D band ranges from  $2,682$  to  $2,688 \text{ cm}^{-1}$  with a FWHM around  $25 \text{ cm}^{-1}$ . This means that these graphene ribbons are strain-free (unlike EG grown on the Si-face of SiC). This is confirmed by the presence of wrinkles evidenced by AFM [65]. For such graphene monolayers, the absolute value of the Fermi level (and the doping level) can be extracted from the ratio  $I_G/I_{2D}$  between the integrated intensities of the G band and the 2D band [69]<sup>1</sup>:

$$|E_f| = \frac{\gamma_{ep}}{0.06} \left( \sqrt{\frac{I_G}{I_{2D}} \frac{1}{0.26}} - 1 \right) \quad (2.18)$$

$$|n| = \frac{1}{\pi} \left( \frac{E_f}{\hbar v_0} \right)^2 \quad (2.19)$$

In these equations,  $\gamma_{ep} = 21 \text{ meV}$  is proportional to the electron–phonon scattering rate [70],  $v_0 = 10^6 \text{ m s}^{-1}$  is the electron velocity. The 0.06 factor is deduced from the function  $f(r_S)$  [69] by using the effective dielectric constant  $\epsilon_{\text{eff}} = 5.33$  for our graphene layer comprised between air and 6H SiC ( $\epsilon_{6\text{H-SiC}} = 9.66$  [71]). The absolute value of the Fermi level was then evaluated for all data points collected on the right ribbon (see Fig. 2.4), giving absolute values between 200 and 350 meV. This corresponds with a doping level between  $3 \times 10^{12}$  and  $9 \times 10^{12} \text{ cm}^{-2}$  with an average of  $6 \times 10^{12} \text{ cm}^{-2}$ . We have not checked directly on the same ribbon but transport measurements performed on similar ones [27] gave a hole concentration of  $5 \times 10^{12} \text{ cm}^{-2}$ . Such a concentration is in excellent agreement with the G and 2D band positions [72].

Concerning the second ribbon (on the left side), as already said we found a twice larger relative extinction. Ranging from 2.6 to 2.8 %, it indicates a bilayer system. The relative extinction and the G band intensity both indicate that this ribbon is a bilayer with an excellent thickness uniformity. On the contrary, the 2D band intensity map in Fig. 2.4 reveals sharp variations and, basically, the ribbon can be divided into three different domains: the top and bottom part having a less intense 2D band intensity than the middle one. Since these variations are correlated with shifts of the 2D and G bands positions, we assume that there are some doping level fluctuations. Indeed, it has been recently demonstrated that the G Raman band depends strongly on its electrostatic environment [73, 74]. If the top graphene sheet has a different doping level than the bottom one, the doping difference changes the Raman shift and intensity of the G band. It also breaks the inversion symmetry and activates antisymmetric modes (that are usually Raman inactive). This results in a splitting of the G band which was observed experimentally [75–77]. Our interpretation is

<sup>1</sup> The ratio between the integrated intensities of the 2D and G band depends on the experimental setup. In our case  $I_{2D}/I_G = 1.02$  for our HOPG reference sample. For the lack of a better knowledge, we assume that our setup is similar to the ones of Refs. [69, 70].

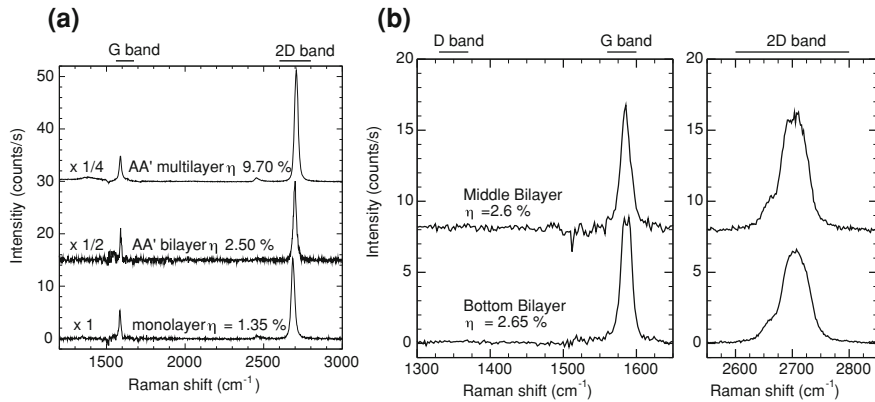


**Fig. 2.5** **a** Raman spectra of different ribbons: a monolayer, a misoriented bilayer and a turbostratic multilayer with their corresponding relative extinction. A misoriented bilayer has a similar Raman spectrum than a monolayer with a twice intensity. The multilayer corresponds to eight graphene sheets that are all disoriented with respect to each other. Therefore the single Lorentzian shape of the 2D band cannot be used as a proof to assert the monolayer character of a FLG sample; **b** Raman spectra of different area of the AB bilayer ribbon. One is extracted from the bottom, the second from the middle of the ribbon. The bottom part of the ribbon exhibits a double G peak that can correspond to a different doping level between the top and bottom graphene sheet

strengthened by the two Raman spectra shown in Fig. 2.5b. In both cases, the 2D band exhibits the characteristic shape of AB (Bernal) stacking [68] but the G band is different. On the upper spectrum a single G peak is observed while on the lower one (collected in the bottom part of the ribbon) a clear G band splitting shows that both layers are not evenly doped.

Bernal stacking is not that usual for EG grown on the C-face of SiC substrates. Most of the time the graphene planes are slightly misoriented, corresponding to turbostratic stacking. In this work, we also found misoriented ribbons (not shown). The presence of rotational stacking faults between the two (or more) successive graphene planes results in Raman spectra similar to the monolayer one as shown in Fig. 2.5a. The line shape is not modified. Simply the intensity increases as the number of graphene sheets increases. In Fig. 2.5a we mentioned the relative extinction measured on these ribbons. We found 2.5 and 9.7 % that corresponds respectively to a bilayer and a 7 or 8 misoriented layers stack. These spectra correspond to FLG where all graphene sheets are disoriented with respect to each other. The spectra of folded Bernal stacked multilayers can be even more complex [78]. Therefore, the fact that the 2D band has a single Lorentzian shape can definitively not be used as a proof to assert the monolayer character of FLG flakes. The combination of  $\mu$ RS with micro-transmission measurements appears then as a most necessary tool to discriminate (without any ambiguity) between true MLG and misoriented multilayers. Of course, to perform such reproducible intensity measurements, any laser power fluctuation has to be carefully corrected. In this work, this was done using an additional low noise photodiode that measured continuously the laser power during the Raman map acquisitions.



## Raman Imaging of FLG Grown on the Si-Face

In Fig. 2.6, we show an optical microscope (OM) image and two  $30 \times 40 \mu\text{m}^2$  micro-Raman maps collected on an EG stack grown on the Si-face of a 6H-SiC substrate. On the first map, the normalized integrated intensity of the G band is shown and compared to the Raman shift on the second map. On the OM image, we can distinguish three different features: black points that correspond to thick graphitic pits, dark areas that correspond to the central parts of the terraces while the bright areas correspond to the edges of the step bunched SiC reconstructed surface. The terraces are  $5 \mu\text{m}$  wide and  $10 \text{nm}$  high and, from the G band intensity, we find that graphene covers all the SiC surface. It is then impossible to measure directly the relative extinction and (consequently) the FLG thickness. An alternate method is to evaluate the thickness from the normalized integrated intensity of the G band, assuming that the average G band normalized intensity of a monolayer is between 0.025 and 0.03. Beware that these values depend on the experimental configuration and must be calibrated. For thin FLG (less than five layers) the error can be of 1 layer and, for thicker FLGs, the estimated thickness may have a factor two error. Unlike the G band, the 2D band intensity cannot be used to evaluate the thickness for the reasons discussed before. The 2D band intensity strongly depends on the stacking for multilayers and on the Fermi level for monolayers [69]. In this way, one finds about 5 layers in the center of terraces (green-blue areas in Fig. 2.6) and about 11 layers on the stripes close to the edge of terraces. On the black points of the optical image, the G band intensity is much intense. This means that they correspond to thick graphitic pits. The Raman spectra of these pits exhibit a strong D band, characteristic of a bad crystalline quality. Such pits are probably induced by an increased growth rate coming from the presence of structural defects, like threading dislocations, in the SiC wafer.

Raman spectra collected in the middle of the terraces and on the stripes are shown in Fig. 2.7a. Unlike the graphitic pits, no D band can be observed. This shows that most of the grown FLG have an excellent crystalline quality. The 2D band is broad with a lower frequency shoulder. This shoulder is more pronounced for the thickest FLG which have a 2D band shape similar to the HOPG one. This asymmetric 2D band is a clear indication of Bernal stacking even for the thinner FLG, where the low-frequency shoulder is known to become less visible [79].

These Raman spectra also reveal that both G and 2D bands are shifted to high frequencies. For the thinnest FLG the G band falls between  $1,590$  and  $1,600 \text{cm}^{-1}$  and the 2D band between  $2,750$  and  $2,760 \text{cm}^{-1}$ . Such high blueshift cannot be explained by doping but rather by a compressive stress experienced by the FLGs. This stress comes from the differential dilatation coefficient between the FLG and the SiC substrate when cooling down the sample after the growth. Thanks to the Grüneisen parameters that have been recently measured [80, 81], this biaxial stress/strain can be estimated from the coefficients listed in Table 2.2. We find strain values between  $-0.3$  and  $-0.4 \%$ , corresponding to local stress values ranging from  $-3$  and  $-5 \text{GPa}$ . However, for thicker FLGs, the G and 2D band are less shifted. This reveals a partial strain relaxation as the graphene thickness increases, which can be easily seen in Figs. 2.6 and 2.7a. The thicker the FLG, the less blueshifted the spectrum.



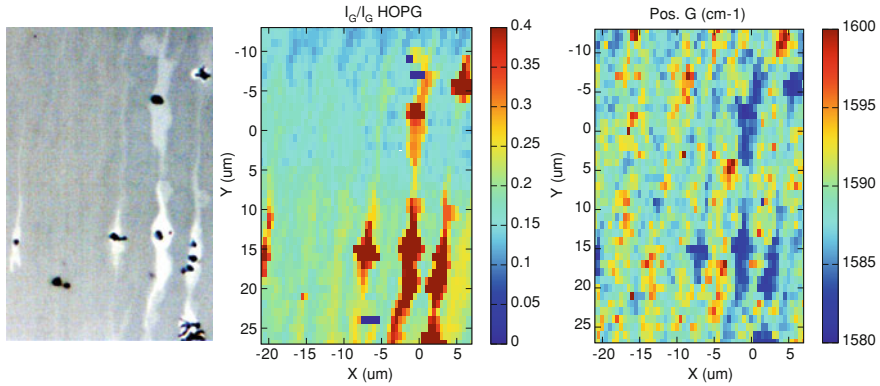


**Fig. 2.6**  $30 \times 40 \mu\text{m}^2$  optical image of the graphene surface and the corresponding Raman maps of the G band intensity and Raman shift. The intensity of the G band is integrated and normalized by the G band of an HOPG reference sample. A full graphene coverage of the surface is observed with thickness inhomogeneities. FLG are thicker at the step edges (about 11 layers) than in the middle of the terraces (about 5 layers). On the edges we can clearly observe stripes: *bright areas* on the OM image and *red areas* on the G band intensity map. On the OM image, we can also see *black points* that correspond to C-rich graphite pits induced by an increased growth rate due to the presence of crystalline defects. On the G band intensity map, *blue points* mark the presence of Si clusters where the Raman fingerprint of silicon was observed. Finally, the G band is shifted to higher frequencies indicating that FLG are compressively stressed. This stress is progressively relaxed as FLG are thicker

**Table 2.2** Frequency shifts of the G and 2D bands for a biaxial strain of 1 % or a biaxial stress of 1 GPa [80, 81]

$\varepsilon_{\text{biax}} = 1 \%$	$\sigma_{\text{biax}} = 1 \text{ GPa}$
$\Delta\omega_{\text{G}}^{\text{biax}} = -60 \text{ cm}^{-1}$	$\Delta\omega_{\text{G}}^{\text{biax}} = -4.8 \text{ cm}^{-1}$
$\Delta\omega_{\text{2D}}^{\text{biax}} = -153 \text{ cm}^{-1}$	$\Delta\omega_{\text{2D}}^{\text{biax}} = -12.3 \text{ cm}^{-1}$

From these results, we confirm that there is a strong difference between graphene grown on the C-face and graphene grown on the Si-face of SiC substrates. On the Si-face graphene strongly interacts with the underlying SiC lattice. This interaction leads to the formation of the so-called buffer layer, which is covalently bound to the SiC lattice [60, 82]. This buffer layer interacts also with the graphene layers that are grown subsequently. It induces a downward shift ( $E_{\text{D}} = -0.4 \text{ eV}$ ) of the K point corresponding to a *n*-type doping. This interaction causes also deviations from the linear band dispersion leading to a parabolic dispersion with an apparent gap of  $\sim 0.25 \text{ eV}$ . This strong interaction is also responsible for the thermal stress experienced by these graphene layers. This is no longer true for the C-face, on which it has been shown that graphene interacts very weakly with the underlying substrate [63, 64]. This is the weakness of this interaction that explains why rotational stacking faults can easily occur and why the graphene sheets can relax the thermal stress by forming wrinkles or pleats.

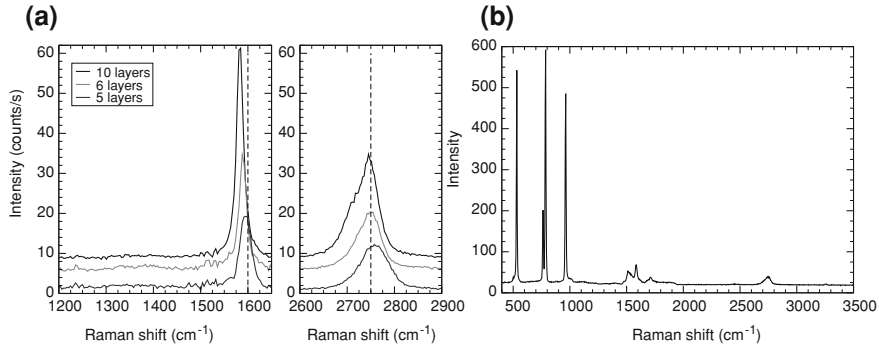


**Fig. 2.7** **a** Raman spectra collected in the middle of the terraces (5–6 layers) and on the stripes close to the step edges (11 layers). No D band can be observed confirming the excellent crystalline quality of these FLG. The asymmetric shape of the 2D band (that is more pronounced for the thicker FLG) reveals a Bernal stacking of the graphene planes. Finally, both bands are *blueshifted*. Such shift can only be explained by a compressive strain of the graphene lattice coming from the differential dilatation during the cooling down of the sample. A partial strain relaxation occurs for thicker FLG since the thicker the less shifted; **b** uncorrected Raman spectrum extracted from the Raman mapping that corresponds to one of the *blue point* in the G band intensity map. The first-order Raman scattering of SiC correspond to the bands at 764, 786, and 964  $\text{cm}^{-1}$ . Its second overtone falls between 1,400 and 2,000  $\text{cm}^{-1}$  with the sharp G band around 1,590  $\text{cm}^{-1}$ . The 2D band is around 2,780  $\text{cm}^{-1}$ . No D band can be seen on this point. The sharp and intense band around 532  $\text{cm}^{-1}$  correspond to a crystalline Si cluster that is highly compressively stressed by the SiC substrate

Finally, on the G band intensity map we can see several points marked in blue. These blue points correspond to area where crystalline silicon clusters were found. One of the corresponding uncorrected Raman spectrum is shown in Fig. 2.7b. The presence of these crystalline silicon (c-Si) clusters is evidenced by the sharp and intense band around 532  $\text{cm}^{-1}$  blueshifted compared to bulk silicon. This high blueshift is again due to a strong compressive stress induced by the SiC substrate (−2 GPa or a strain of −1.3 %). First-order Raman scattering of the SiC substrate corresponds to the two TO modes of  $E_2$  symmetry at 764 and 786  $\text{cm}^{-1}$  and the  $A_1(\text{LO})$  phonon at 964  $\text{cm}^{-1}$ . Its second overtone with its characteristic fingerprint [83] falls between 1,400 and 2,000  $\text{cm}^{-1}$  under the sharp G band of FLG around 1,590  $\text{cm}^{-1}$ . The 2D band is around 2,780  $\text{cm}^{-1}$ . No D band can be seen on these points. Moreover, we can see that no significant variations of the G band intensity and Raman shift can be observed close to these Si clusters. This means that these Si clusters do not alter the graphene growth. These clusters are located close to the step edges, like the graphitic pits. There might be a link between the presence of different defects at the step edges like these clusters, the higher growth rate, and the clear electrical anisotropy that has been evidenced by magnetoresistance experiments performed on several Hall bars with different orientations [66].

Summarizing: from recent Raman imaging experiments performed on EG grown on the C and Si face of 6H SiC substrates, we have shown the benefits of combining

Raman spectroscopy with micro-transmissions measurements. Provided the relative extinction of FLGs can be obtained, this enables to determine (without any ambiguity) the thickness, homogeneity, and stacking order (Bernal or turbostratic). On the C-face of SiC substrates we have shown that long, self-ordered, graphene ribbons can be grown. These ribbons have excellent crystalline quality and are strain relaxed. They are up to 600  $\mu\text{m}$  long and 5  $\mu\text{m}$  wide. They are mainly monolayers and Bernal stacked bilayers but turbostratic bi and multilayer areas have also been found. Finally and for monolayers graphene, we also illustrated how the absolute value of the Fermi level can be found, in good agreement with electrical results. On the opposite, on the Si face, a full graphene coverage of the SiC surface has been found. The surface is still heavily step bunched but a high compressive thermal strain and  $n$ -type doping was observed. It confirms that on the Si face a strong interaction exists between the graphene layers and the underlying SiC substrate. FLG on the Si face exhibit Bernal stacking with thickness inhomogeneity. Thin (5 layers) FLGs were grown in the middle of terraces, while thicker graphene stripes grew close to the step edges. In the vicinity of these steps disordered graphite pits and crystalline Si clusters were found. There might be a link between the presence of these defects, the thickness inhomogeneity, and the clear electrical anisotropy that has been recently evidenced by magnetoresistance experiments.

### 2.2.3 Strained Silicon Wafers Manufacturing

Many advanced substrates have been developed recently, based on the idea of integrating any semiconductor with silicon (Anything on Si). This is a very attractive idea, since the technologies developed on these semiconductors would become directly compatible with the mainstream Si technology. Among these new “engineered” or “smart” materials, epitaxial  $\text{Si}_{1-x}\text{Ge}_x/\text{Si}$  heterostructures have attracted considerable interest, because of the possibility to enhance the performances of complementary metal oxide semiconductor (CMOS) devices. This is a very important point since, for a long time, the performance improvements have been done by miniaturizing individual devices. Unfortunately, this so-called scaling down technology is facing significant physical and economical limitations. As a consequence, since the 90 nm technology node, an alternative approach called “strain engineering” has been incorporated to maintain the Moore’s law predictions.

As a matter of fact, introducing strain in the active region of a device results in large mobility enhancement of, both, the electrons and holes. Such strained film can be either strained Si (sSi), strained Ge (sGe), or even strained SiGe Alloys (sSiGe). This depends only on the final application: MOSFETs, SiGe-based heterojunction bipolar transistors (HBT), optoelectronic devices like optical waveguide, quantum well infrared detectors, and quantum cascade emitters [85–92].

Basically, two types of techniques can be used for strain introduction. First, the “global strain” approach uses a wafer with a sSi film on top. This can be either sSi on a SiGe virtual substrate or sSi on SiGe on Insulator or sSi on Insulator. These three

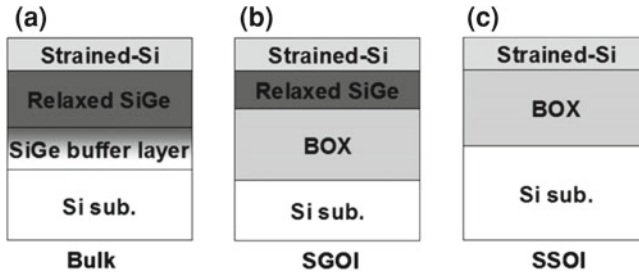


**Fig. 2.8** Schematic drawing of three types of wafers used for introducing strain in the channel of field effect transistors. **a** A strained silicon film is grown on top of a relaxed SiGe layer. The relaxation of the SiGe layer is made by growing a graded buffer with an increasing Ge content; **b** SGOI wafer with a sSi film on a relaxed SiGe layer on an insulator (silicon oxide); **c** sSOI wafers are made of a strained silicon film on top of a buried oxide layer. Reprinted from [84]. Copyright 2007, with permission from Elsevier

wafer stacks are sketched in Fig. 2.8 in which, every time, the sSi film is produced by growing a thin Si layer on top of a strain-relaxed SiGe buffer layer (virtual substrate). The second technique, called “local strain” approach, consists in introducing strain in a selected region during LSI fabrication. It will be discussed in the next section.

Focusing on the first “global strain” approach, and whatever is the final option, the fabrication of this virtual substrate is a key issue. Indeed, the properties of the overgrown Si film are strongly influenced by the quality of the buffer layer and, since the strain relaxation of the SiGe buffer layer (grown on a Si handle wafer) generates dislocations, several techniques have been developed to prevent dislocation extension to the surface. The most established ones are using a compositional graded buffer [94] or a low-temperature buffer layer [95]. In both cases, they lead to threading dislocations density below  $10^{-5} \text{ cm}^{-2}$ .

### Bulk sSi/Si<sub>1-x</sub>Ge<sub>x</sub>/Si Heterostructures

The ability to control (and monitor) the composition and relaxation of a SiGe alloy is crucial to improve the growth process and engineer the electrical and optical properties of the final heterostructures. In this case, since the frequencies of the alloy Raman peaks depend on the composition,  $\mu\text{RS}$  is of great interest and has been used as a straightforward tool to determine the depth profile of the alloy composition.

Basically, depth profiling in Raman imaging can be done in several ways. The first one uses different laser wavelengths to change the penetration depth of the incident beam and the Raman cross-section. In this way, depth profiles of stress [96, 97] and lattice damage in annealed GaAs [98] have been measured. The second one is based on confocal microscopy and consists in moving the sample vertically [99]. The third one consists in measuring the Raman profile along a cross-section of the sample, on a cleaved or bevelled surface. This method is destructive but gives a very

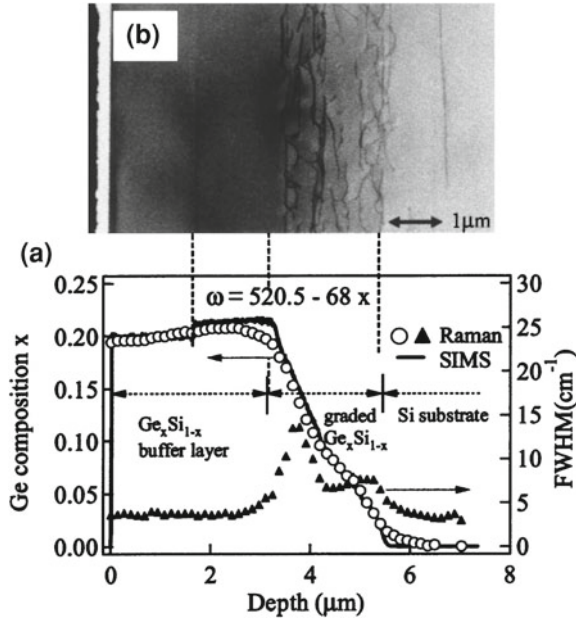


**Fig. 2.9** Characterization of the depth profile of a strained silicon film grown on a relaxed  $\text{Si}_{0.8}\text{Ge}_{0.2}$  virtual substrate. Raman image has been acquired on the cleaved surface of the graded buffer. **a** The Ge composition determined from Raman and SIMS analyses are plotted against the depth position and are in perfect agreement. The Raman linewidth of the Si-Si Raman mode is also represented against the depth position. The broadening has maxima at the lower and upper parts of the graded layer. It comes from the high density of dislocations evidenced by the **b** cross-sectional TEM image of the same structure. Reprinted with permission from [93]. Copyright 2004, American Institute of Physics

detailed image of the in-depth stress profile in SOI substrates [100–105]. It has been also used to study heteroepitaxial InAs grown on GaAs or InP substrates [106], the carrier density at the ZnSe/GaAs interface [107], and even to image quantum wells [108–110].

Concerning sSi/SiGe/Si, Nakashima et al. [93] applied the cross-section technique to study the growth of a strained Si film on top of a relaxed SiGe virtual substrate. The main concern was to determine the depth profile of the Ge composition in the graded buffer and in the uniform SiGe buffer layers. They combined  $\mu\text{RS}$  with cross-sectional transmission electron microscopy (TEM) and secondary ion mass spectroscopy (SIMS) to determine the Ge content of the SiGe alloys and to study its crystalline quality. The results are shown in Fig. 2.9. Assuming that the strain is completely relaxed in the SiGe layer, the shift of the Raman frequency  $\omega_{\text{Si-Si}}$  of the Si-Si Raman peak was used to determine the Ge content  $x$  through the relationship (see Sect. 2.1.1):

$$\omega_{\text{Si-Si}} = 520.5 - 68x \quad (2.20)$$

Results are shown in Fig. 2.9a. The Ge composition and the broadening of the Si-Si Raman mode are plotted against the depth as white circles and black triangles, respectively. Notice that the composition determined by Raman spectroscopy (open dots) is in excellent agreement with the one obtained by SIMS (full line). On top of the SiGe virtual substrate, the Raman Si-Si peak reaches a frequency of  $507\text{ cm}^{-1}$  which is nearly equal to the frequency of an unstrained  $\text{Si}_{0.8}\text{Ge}_{0.2}$  layer. They also checked by UV Raman spectroscopy that the top Si film was fully strained. These two observations and the cross-sectional TEM image shown in Fig. 2.9b confirm the relaxation of the SiGe layer that occurs through the nucleation of misfit dislocations.

The TEM image clearly shows that most of the dislocations are concentrated in the lower and upper regions of the graded  $\text{Si}_{1-x}\text{Ge}_x$  layer. This high density of crystalline defects explains the broadening of the Si-Si Raman mode. This is shown in Fig. 2.9a. Notice that the bandwidth has maxima at the lower and upper parts of the graded layer, while, in the Si wafer, the  $\text{Si}_{1-x}\text{Ge}_x$  buffer layer and the top sSi film, the bandwidth decreases. Basically, the broadening comes from two contributions. One is the inhomogeneous broadening due to the laser spot size (about  $1\text{ }\mu\text{m}$ ) which corresponds to the superposition of Raman signals coming from regions of different Ge composition. Nakashima et al. estimated this contribution around  $3\text{ cm}^{-1}$ , which is much smaller than the measured value. The second contribution comes from the broadening induced by the defects. As the lattice loses translation symmetry, the wave vector conservation breaks down and the photons can be scattered by phonons that have wavevectors far away from the zone center. This happens in mildly imperfect crystals with a small concentration of defects or in solid solutions, alloys, and amorphous solids [6]. For lightly disordered lattices, this manifests as an asymmetrical broadening of the Raman peak and, most of the time, the peak broadens at lower frequency [101]. Of course, as the material becomes amorphous, the Raman spectrum consists of a few broad bands which are correlated to the density of states. S. Nakashima et al. used this broadening to estimate qualitatively the crystalline quality of the  $\text{Si}_{1-x}\text{Ge}_x$  alloy. It can also be used to characterize the damage induced by ion implantation in silicon on insulator (SOI) technology [111] or the crystallite size in micro and polycrystalline Si [112].

Up to now, we have seen that the strain relaxation of  $\text{Si}_{1-x}\text{Ge}_x$  alloys involves the generation of misfit dislocations at the SiGe/Si substrate interface [113] and yields surface roughening. The surface has a well-known crosshatch pattern running along orthogonal (110) crystalline directions, which is characteristic of the low misfit regime (lattice mismatch lower than 2%). It is, for instance, easily evidenced by atomic force microscopy observations [114–116] and, in SiGe layers, develops through the combination of two mechanisms which depend on the film thickness: (i) dislocations-induced surface steps due to shear displacements caused by dislocations glide and (ii) the growth of self-organized periodic ridges [117].

To study this crosshatch pattern, Chen et al. [118] performed Raman mapping on a 500 nm thick  $\text{Si}_{0.75}\text{Ge}_{0.25}$  epitaxy grown on top of a 50 nm low temperature Si (LT-Si) buffer layer. The micro-Raman spectra were measured in the backscattering configuration, using the 514.5 nm line of an Ar laser. Such wavelength enables to probe simultaneously the SiGe epitaxial film, the LT-Si layer, and the Si substrate

underneath. As a consequence, the spectra exhibited 4 peaks corresponding to the Si substrate, the Ge-Ge, Si-Ge, and Si-Si bond vibrations in the epitaxial SiGe layer. The frequency maps of these peaks evidenced clearly the crosshatch pattern along the (110) crystalline directions and they demonstrated that the frequency shifts were due to strain fluctuations coming directly from misfit dislocations nucleated at the SiGe/Si interface. They also demonstrated that the Ge composition of the SiGe layer was uniform and independent of these strain undulations.

Following this first series of experiments, Sawano et al. [119–122] showed that this crosshatch morphology is almost the same for the surface roughness evidenced by AFM and for the in-plane strain distribution observed by Raman imaging. This inhomogeneous strain field comes from the underlying misfit dislocation and exists all over the SiGe film even after surface planarization made by chemical mechanical polishing (CMP). It exists also in sSi layers grown on a thick SiGe virtual substrate. Strain fluctuation and surface roughness, particularly its wavelength, depend strongly on the buffer thickness: the thicker the buffer, the longer the crosshatch wavelength. Since TEM experiments indicate that the misfit dislocation network is confined in the SiGe graded layer, this means that the crosshatch wavelength depends only on the distance between the surface and the dislocation network. The crosshatch surface roughness appears again after homoepitaxial regrowth of SiGe on planarized SiGe buffer layers because the growth kinetics and especially the surface diffusion of adatoms is perturbed by the strain field fluctuation existing on the SiGe surface. Therefore, increasing the buffer thickness does definitely not solve this issue. Although, the wavelength increases and the uniformity is improved, long range strain fluctuation still exists on buffer layers as thick as 7  $\mu\text{m}$ .

## Strained Silicon Films on Insulator

Strained silicon films on SiGe epilayers on bulk Si substrates suffer from technological limitations coming (most of the time) from the graded buffer layer. In this case, Ge diffusion, strain relaxation, nucleation, and migration of misfit and threading dislocations are some of the issues that limit the flexibility of CMOS integration. To overcome these limitations, merging strained silicon with SOI technologies has been suggested [123]. This has many advantages. For partially depleted SOI device architectures, relaxed SiGe on insulator with a tensile strained silicon layer on top (SGOI wafers in Fig. 2.8) can boost circuit performance up to 30 % while tensile-strained silicon directly on insulator (sSOI wafers in Fig. 2.8) combines the performance and scalability of fully depleted ultra-thin SOI with the mobility enhancement of strained silicon.

Several technologies allow producing such hybrid substrates. The preferred one is the so-called Smart Cut<sup>TM</sup> technology patented by SOITEC for mass production of SOI wafers. It uses hydrogen implantation to form a buried (weakened) zone in a so-called donor wafer A. Then wafer A is bonded to an handle wafer B by wafer bonding. Prior to the bonding step, an insulating layer such as SiO<sub>2</sub> is formed at least on one of the two wafers. The splitting step that follows occurs inside the weakened



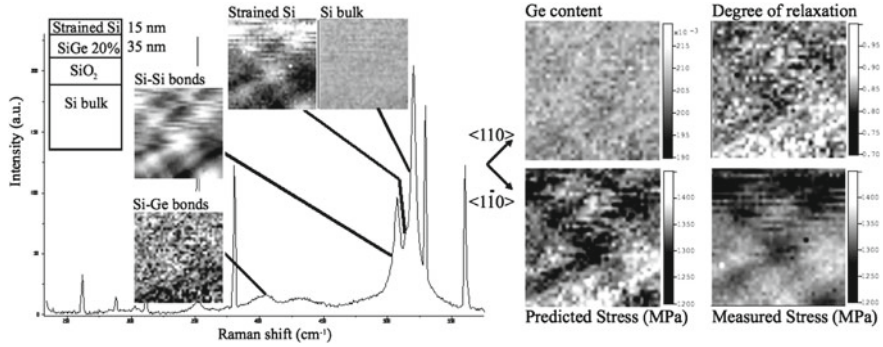


**Fig. 2.10** Raman spectrum collected on a SGOI wafer. The wafer composition is sketched in the *upper left corner*. Starting from the high frequencies, we clearly observe the Raman modes of the bulk Si substrate, the strained Si cap, the Si-Si and Si-Ge bond vibrations in the relaxed  $\text{Si}_{0.8}\text{Ge}_{0.2}$ . The *sharp lines* correspond to Rayleigh scattered plasma lines of the Argon laser. They are used for frequency calibration. From a  $20 \times 20 \mu\text{m}^2$  Raman mapping, one determines from the frequency of each mode, the Ge content, the degree of relaxation of the SiGe layer, and the stress in the strained Si film. All the maps except the Ge content exhibit clearly the crosshatch pattern. This pattern comes from the network of the misfit dislocations that nucleate during the SiGe growth. It manifests itself by a roughening of the SiGe surface, and by a strain fluctuation in the SiGe lattice. This strain fluctuation is kept after the layer transfer process in the SGOI wafers. From the SiGe layer properties, one calculates the SiGe lattice constant and predicts the stress in the strained Si cap. In the *bottom maps*, we compare the predicted and measured stress. The stress difference is lower than 100 MPa for all points of the map. It confirms the perfect lattice matching between the SiGe and the sSi films without misfit dislocation nucleation [124]

zone and gives rise to the transfer of a thin layer from the donor substrate A onto the handle wafer B. A final treatment removes the rough surface left after splitting. This concept can be applied to almost any semiconductor such as: Si, SiC, GaN, GaAs, InP, SiGe, Ge, ... to obtain combinations of interest like: SOI, SOQ, GaNOI, SiCOI, GaAs/Si, InP/Si, etc....

To produce SGOI or sSOI wafers, the donor substrates are, respectively, a relaxed SiGe virtual substrates or a strained Si film on top of a relaxed SiGe virtual substrate. The final stacks are sketched in Fig. 2.8. To produce a SGOI wafer, only a thin part of the relaxed SiGe buffer is transferred, followed by a strained silicon film epitaxy. For sSOI wafers, a bilayer containing the strained Si and the relaxed SiGe films is transferred. The remaining SiGe film is removed by selective etching (for instance).

One can wonder how this layer transfer technology affects the strain field coming from the crosshatch. Indeed, since the misfit dislocation network is not transferred in the SGOI and sSOI wafers, this is not obvious. To answer this question, Raman mapping on donor wafers with a strained Si cap and on SGOI wafers have been done [124]. Typical results are shown in Fig. 2.10. The measurements were done using the 488 nm line of an Ar laser which enabled to probe the strained Si cap, the  $\text{Si}_{0.8}\text{Ge}_{0.2}$  film, and the handle Si substrate simultaneously. The Raman maps were  $20 \times 20 \mu\text{m}^2$  large. Raman shifts variations of both film (SiGe and strained Si) exhibited the same



crosshatch pattern as the one observed on the donor wafer. From these Raman shifts, we determined the stress in the strained Si film, the Ge content  $x$ , and the degree of relaxation of the SiGe layer through the following relationships [124]:

$$\omega_{\text{Si-Si}} = 521 - 68x - 815\epsilon_{\parallel} \quad (2.21)$$

$$\omega_{\text{Si-Ge}} = 399.5 + 14.2x - 575\epsilon_{\parallel} \quad (2.22)$$

while the degree of relaxation is given by:

$$\text{degree of relaxation} = 1 - \frac{\epsilon_{\parallel\text{exp}}}{\epsilon_{\parallel\text{th}}} \quad (2.23)$$

In these expressions,  $\epsilon_{\parallel\text{exp}}$  is the residual strain measured in the SiGe layer and  $\epsilon_{\parallel\text{th}}$  is the theoretical strain of a fully strained  $\text{Si}_{1-x}\text{Ge}_x$  layer grown on a Si substrate.

It should be noticed that a controversy still exists concerning the exact values of the numerical coefficients [125–127] and that the Eq. 2.22 is only valid for Ge content lower than 30 %. Moreover, the Si-Ge frequency does not vary linearly versus Ge content [128]. The Ge content  $x$  and the degree of relaxation of the SiGe maps are shown in Fig. 2.10. These results confirm that the Raman shift variations come only from strain modulation in the SiGe layer and not from a composition fluctuation. This strain network remains in the SGOI wafer and also in the sSOI wafers (see Fig. 2.11c) even in the absence of the misfit dislocation network. They also confirm the influence of the strain modulation induced by the dislocations on the growth kinetics of the SiGe and strained Si films.

From the SiGe composition and its degree of relaxation, the SiGe in-plane lattice parameter was deduced. Assuming that the sSi film is grown with perfect lattice matching, its in-plane lattice parameter should be the same as the SiGe one. Therefore, one can deduce the induced strain/stress of the strained Si cap. This predicted stress is compared to the experimental one in Fig. 2.10. Notice the very good agreement with a stress difference lower than 100 MPa. This confirms the perfect lattice matching between the Si cap and the strain relaxed SiGe buffer. It was also observed that the bulk substrate was subjected to a small in-plane tensile stress (around 100 MPa) due to the high-temperature annealing steps and the difference between the thermal expansion coefficients of the buried oxide and silicon [102–105].

## UV Raman Approach

Until now, we have seen that the strain field induced by the network misfit dislocations affects the local growth rate. It causes also the crosshatch surface roughening which remains in SGOI and sSOI wafers after layer transfer. As this strain field might also impact the process parameters used to manufacture the devices (and therefore their performances [129, 130]), it is crucial to develop characterization tools that can monitor the strain field continuously before and during the device fabrication.

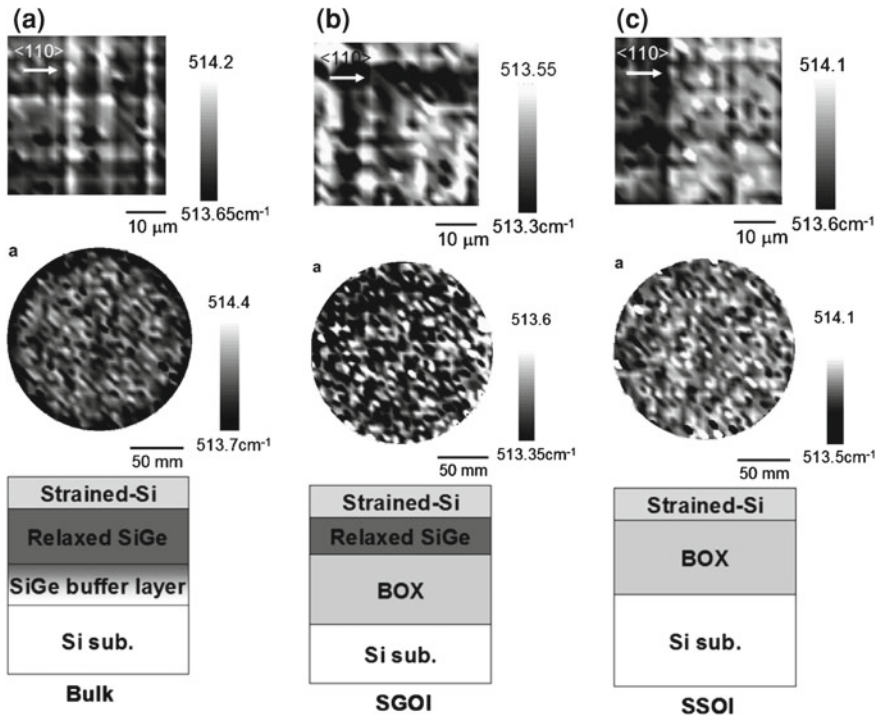


**Fig. 2.11**  $40 \times 40 \mu\text{m}^2$  and full wafer map of the Raman frequency of the strained Si layer measured on 200 mm wafers of **a** strained Si on a relaxed SiGe virtual substrate; **b** SGOI; **c** sSOI. We clearly observe the crosshatch pattern on the  $40 \times 40 \mu\text{m}^2$  maps. It shows that the strain network induced by the misfit dislocations network is kept after the layer transfer process step. The Raman mode of the strained silicon film exhibits a  $0.6 \text{ cm}^{-1}$  frequency fluctuations. The same fluctuations are observed for the full wafer map of the 200 mm wafers. We can deduce from these measurements that the strain is almost uniform across the surface of the wafer. It is indeed impossible to discriminate on the full wafer map if the strain fluctuations come only from the crosshatch strain modulation or from long range wafer inhomogeneities. Reprinted from [84]. Copyright 2007, with permission from Elsevier

To answer this need Ogura et al. [131] built a specific UV-Raman setup. Basically, the 363.8 nm line of an Ar laser is focused by a 90x objective lens giving a spatial resolution of  $0.5 \mu\text{m}$ . A  $300 \times 400 \text{ mm}^2$  translation stage combined to an autofocus system enabled to map 12 in wafers. A high resolution spectrograph (2 m focal length) is coupled to a charge couple device (CCD) detector and a dual focusing mirror was used to perform real-time calibration of the laser frequency. The dual concave mirror enabled to measure simultaneously (on the same CCD detector) the Raman signal coming from the wafer and the Rayleigh scattering of the incident laser which was used as an internal frequency reference. Finally, to ensure a good reproducibility and repeatability, no optic (including mechanical components in the spectrograph) was moved during the measurement. The spectral resolution obtained was  $0.1 \text{ cm}^{-1}$ .

An important point to notice is that the 363.8 nm line of the Ar laser is (by far) the best one to perform Raman imaging of a thin silicon film. The penetration depth is less than 10 nm and the wavelength corresponds to a very efficient resonant Raman scattering process [132]. The Raman cross-sections is almost 100 times higher than for the visible lines of the Ar laser and 10 times higher than for the 325 nm line of an HeCd laser. This intense signal enables to reduce the acquisition time to few seconds and therefore to perform fast Raman mapping of  $40 \times 40 \mu\text{m}^2$  and of the whole wafer surface. Figure 2.11 displays several examples of mappings collected on a strained Si on a relaxed SiGe virtual substrate, a SGOI, and a sSOI wafer. We clearly observe the crosshatch pattern on the  $40 \times 40 \mu\text{m}^2$  maps. The Raman mode of the strained silicon film exhibits a  $0.6 \text{ cm}^{-1}$  frequency fluctuations. The same fluctuations are observed for the full wafer map of the 200 mm wafers. This image was obtained by collecting a Raman spectrum every 5 mm. More than 1,000 spectra were acquired. We can deduce from these measurements that the strain is almost uniform across the surface of the wafer. It is indeed impossible to discriminate on the full wafer map if the strain fluctuations come only from the crosshatch strain modulation or from long range wafer inhomogeneities. To get a better image of the strain homogeneity across the wafer, the crosshatch strain fluctuations must be averaged either by performing  $40 \times 40 \mu\text{m}^2$  maps each 5 mm, or by illuminating the same  $40 \times 40 \mu\text{m}^2$  surface with galvano mirrors vibrating at high frequency. They also studied the influence of rapid thermal annealing on these wafers with the same system [84]. It has been shown that the sSOI wafers properties remains almost unchanged after high temperature annealing [84, 123]. This is not the case for SGOI and SiGe virtual substrate since Ge diffusion takes place. Finally, recent results [133] report that relaxed SiGe layers can be realized by heavy ion implantation without the formation of crosshatch strain fluctuations.

## 2.3 Stress Monitoring in Production Lines

Mechanical stress has always been a major concern for integrated circuits (IC) technology because of the detrimental effect on devices performance and integrity. Indeed, many problems of defective ICs can be ascribed to stress-induced defects generated during device manufacturing: nucleation and propagation of dislocations, voids, and cracks around local oxidation structures (LOCOS) or shallow trench isolation (STI) [29, 30, 134–136], open or short-circuits failures in interconnection metal lines due to crack, voids and hillock formation. These reliability issues became even more challenging with the constant trend in device downscaling. As Raman imaging is a nondestructive and a relatively fast technique, it has been used for routine analyses and to help designers at the early stage of device development. As already mentioned in the preceding section, the step further was to incorporate strain engineering in the ITRS roadmap [32]. In the “local strain” approach, it consists in introducing and controlling the strain in the channel of a field effect transistor (FET). This can be done by almost all elements constituting and surrounding the FETs: SiGe source drain con-

tacts for a uniaxially compressed channel, trench isolations, silicides, silicon nitride spacers which can induce both tensile or compressive stress in the channel [85, 137]. Since strain and stress are now considered as key parameters to improve the device performance, the most popular application of Raman imaging in Microelectronics has become stress measurement. In this section, we focus on two examples: stress measurements around LOCOS and STI structures.

### 2.3.1 Stress Mapping of Local Oxidation Structures

Local oxidation of silicon (LOCOS) is the most popular technique to achieve lateral isolation in very large-scale integration (VLSI) devices. It consists in defining thick isolation regions between small active device parts by growing silicon dioxide in such isolation regions, also called field regions. LOCOS in field regions is achieved by masking the regions where no oxide must be grown with a silicon nitride ( $\text{Si}_3\text{N}_4$ ) layer. Since nitride oxidizes at a much lower rate than silicon, a thick oxide insulating layer is grown in the field regions, while the areas where the active devices are to be fabricated, are not oxidized. The main reasons for the success of LOCOS in semiconductor technology are its simplicity, effectiveness, and compatibility with all other processing steps.

The process sequence involved in LOCOS isolation is as follows. After growing a thin  $\text{SiO}_2$  layer called pad oxide, a  $\text{Si}_3\text{N}_4$  film is deposited and patterned. This defines the oxidation mask. The wafers are next put in an oxidation ambient to grow a rather thick field oxide (FOX) in the regions where the nitride layer was removed. Since oxidation of silicon occurs also laterally, the growing oxide penetrates under the edges of the nitride mask, lifts them up and gives rise to the formation of a specific geometrical feature called “bird’s peak”. At the end of the process, the nitride film is removed and the wafers planarized.

The apparent simplicity of this process hides several technological challenges, in which mechanical stress plays a significant role. For instance, stress influences the diffusion of oxidant species underneath the nitride edges. It can also induce the nucleation of dislocations at the bird’s peak tip [136]. Altogether, this explains why LOCOS structures have been extensively studied by Raman spectroscopy [134, 135, 138–141]. An illustration is given in Fig. 2.12 from [138, 139]. It focuses on the stress field induced by a poly-buffered LOCOS (PBLOCOS) process. PBLOCOS is an alternative LOCOS structure, in which a polycrystalline silicon (poly-Si) film is added between the pad oxide and the silicon nitride film. This  $\text{Si}_3\text{N}_4$ /poly-Si/ $\text{SiO}_2$  sandwich reduces the field oxide encroachment in the active region. The poly-Si film limits the bird’s peak formation, and absorbs the stress from the nitride.

To monitor the stress-induced Raman shift of the Si phonon during the manufacturing of the PBLOCOS, de Wolf et al. measured 1D profile across the  $\text{Si}_3\text{N}_4$  stripe before the field oxidation [138, 139]. They also performed a Raman mapping of  $4 \times 4 \mu\text{m}^2$  active area [134]. A spectrum was recorded each  $0.2 \mu\text{m}$  using the 457.9 nm line of an Ar laser and a DILOR XY-800 spectrometer coupled to a micro-

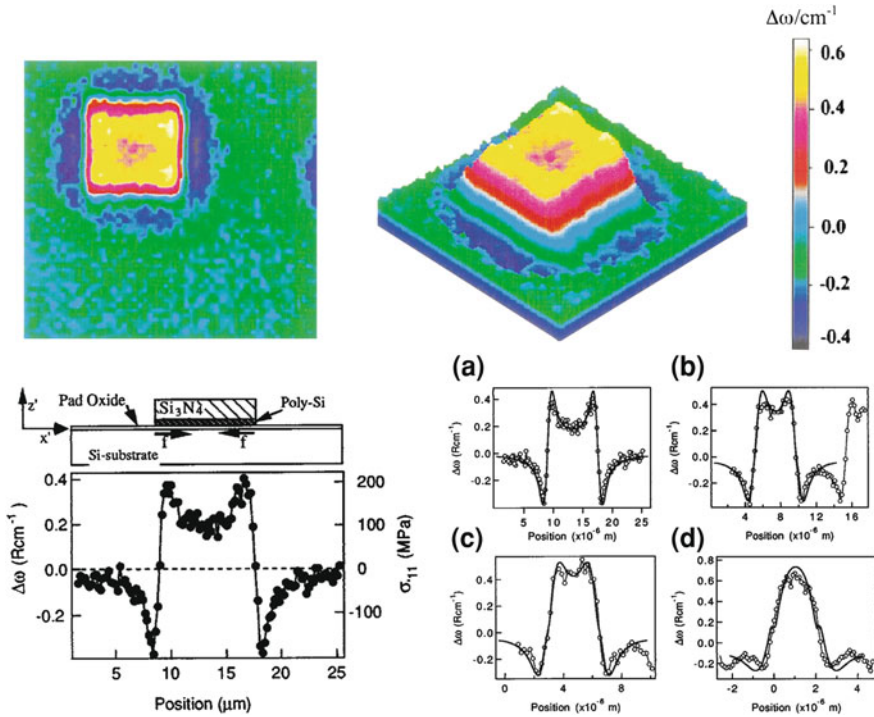


**Fig. 2.12** 2D map of the stress-induced Raman shift of the Si mode measured around a  $4 \times 4 \mu\text{m}^2$  active area surrounded by a PBLOCOS isolation structure. The 2D Raman map was measured across a  $11.5 \times 13 \mu\text{m}^2$  area with a spectrum recorded each  $0.2 \mu\text{m}$ . The Si experiences a tensile stress at the sidewall of the oxide/silicon interface. The edges of the active regions are subjected to a maximum compressive stress that relaxes in the middle of the active region. Reprinted from [134]. Copyright 1999, with permission from Wiley-VCH. 1D profile of the stress-induced Raman shift across the  $\text{Si}_3\text{N}_4$  stripe before the field oxidation for different widths. In the *left hand side* profile, the shift is converted in stress assuming an uniaxial stress along  $x'$  (110). In the *right hand side* profiles (marked a, b, c, d) the *solid line* corresponds to the theoretical shift of the Raman Si mode derived from an analytical model. It gives an excellent agreement with the experimental data plotted with *open circles*. Reprinted with permission from [138, 139]. Copyright 1996, American Institute of Physics

scope and a XY translation stage. To perform such stress measurements, special care must be taken to avoid artifacts. In Fig. 2.12, plasma lines were used to calibrate the spectrometer and the position of the Si Raman peak was evaluated by fitting it with a single Lorentzian function. The 2D Raman map reveals clearly that the shift starts from zero far from the active region and becomes negative ( $\sim -0.3 \text{ cm}^{-1}$ ) in the vicinity of the active region. This tensile stress comes from the sidewall of the oxide/silicon interface and from the bird's peak. In the active region, the stress becomes compressive. It reaches a maximum value at the edge (especially in the corner) and relaxes slightly in the middle of the active region. On the contrary, the

tensile stress is lower around the corner of the active region and maximum near the middle of the edges. The compressive stress in the active region comes from the field oxide and, especially, from its volume expansion during Si oxidation. SiO<sub>2</sub> occupies a volume 2.27 times larger than the original silicon one.

These first qualitative interpretations already help to get an intuitive understanding how the stress develops in such isolation structure. Stress depends directly on the geometry of the device. For instance, the (compressive) stress increases as the slope of the sidewall between the field oxide and the silicon is steeper [134]. Extensive studies have been carried out to investigate how stress is affected by all these geometrical effects, and all the process parameters (temperature, nitride thickness, field and pad oxide thicknesses, oxidation conditions ...). Moreover, to correlate the Raman experiments with standard technology computer-aided design (TCAD) tools, a quantitative value of the stress was derived from the Raman shifts. The standard assumption was to consider that the stress  $\sigma_{xx}$  is uniaxial and aligned along the  $\langle 100 \rangle$  crystalline direction. This case is very similar to the biaxial one treated in Sect. 2.1.4. The phonon polarizations and Raman tensors remain the same as the ones for a relaxed lattice and the frequency shifts are given by:

$$\begin{aligned}\Delta\omega_x &= \frac{pS_{11} + 2qS_{12}}{2\omega_0}\sigma \\ \Delta\omega_y = \Delta\omega_z &= \frac{qS_{11} + (p+q)S_{12}}{2\omega_0}\sigma\end{aligned}\quad (2.24)$$

For pure backscattering from a 001 surface, only the  $\omega_z$  mode is probed. The relationship between the Raman shift and the stress is then:

$$\Delta\omega_z(\text{cm}^{-1}) = -2.3\sigma_{xx}(\text{GPa}) = -300\varepsilon_{xx} \quad (2.25)$$

This assumption cannot be used to evaluate the stress in the 1D profile shown in the lower left corner of Fig. 2.12. This profile was measured across a Si<sub>3</sub>N<sub>4</sub> stripe before the field oxidation. The structure and composition of the stripe is sketched above the Raman profile. Since this stripe is aligned along the  $\langle -110 \rangle$  direction, the preceding assumption is not valid. However, if we assume an uniaxial stress  $\sigma$  aligned along the  $\langle 110 \rangle$  crystalline direction, the strain tensor becomes:

$$\begin{aligned}\varepsilon_{xx} = \varepsilon_{yy} &= \frac{S_{11} + S_{12}}{2}\sigma \\ \varepsilon_{zz} &= S_{12}\sigma \\ \varepsilon_{xy} &= \frac{S_{44}}{4}\sigma \\ \varepsilon_{xz} = \varepsilon_{yz} &= 0\end{aligned}\quad (2.26)$$

Solving the secular equation gives then three different Raman shifts in which the difference with the  $\langle 100 \rangle$  uniaxial stress comes only from the shear component  $\varepsilon_{xy}$ .

$$\begin{aligned}
\Delta\omega_1 &= \frac{(p+q)S_{11} + (p+3q)S_{12} + rS_{44}}{4\omega_0}\sigma \\
\Delta\omega_2 &= \frac{(p+q)S_{11} + (p+3q)S_{12} - rS_{44}}{4\omega_0}\sigma \\
\Delta\omega_3 &= \frac{qS_{11} + (p+q)S_{12}}{2\omega_0}\sigma
\end{aligned} \tag{2.27}$$

associated with polarization vectors:

$$v_1 = \frac{1}{\sqrt{2}} \begin{pmatrix} 1 & 1 & 0 \end{pmatrix} \quad v_2 = \frac{1}{\sqrt{2}} \begin{pmatrix} -1 & 1 & 0 \end{pmatrix} \quad v_3 = \begin{pmatrix} 0 & 0 & 1 \end{pmatrix} \tag{2.28}$$

The Raman tensors become:

$$R_1 = \frac{1}{\sqrt{2}} \begin{pmatrix} 0 & 0 & d \\ 0 & 0 & d \\ d & d & 0 \end{pmatrix} \quad R_2 = \frac{1}{\sqrt{2}} \begin{pmatrix} 0 & 0 & d \\ 0 & 0 & -d \\ d & -d & 0 \end{pmatrix} \quad R_3 = \begin{pmatrix} 0 & d & 0 \\ d & 0 & 0 \\ 0 & 0 & 0 \end{pmatrix} \tag{2.29}$$

With standard backscattering from the 001 surface, only the third mode can be observed which still corresponds to the phonon polarized along the  $z$  axis. Moreover the strain induced shift  $\Delta\omega_z$  remains the same. This latter remark confirms the difficulty in determining the strain tensor from Raman experiments. It is indeed impossible to discriminate if the stress is uniaxial, biaxial and to determine its orientation with respect to the crystalline directions. Using Eq. 2.25 gives only a semiquantitative estimation of the stress in the sample. To get a more accurate determination of the nature and the value of the stress, it is necessary to use a more tedious method. The strain and stress tensors must be determined in all points of the sample probed by Raman imaging. They can be computed by analytical models [136] or by finite element simulations [142]. The next step is then to determine how this stress distribution influences the Raman scattering (frequency shifts, polarization vectors and Raman tensors). The Raman tensors indicate which Raman modes are allowed and give their intensity. The final step is to average the Raman scattering of the probed volume that is given by the penetration depth and the spot size of the laser. “Theoretical” Raman maps can then be determined and compared to the experimental ones.

This procedure was applied to fit the 1D Raman profile recorded across  $\text{Si}_3\text{N}_4$  stripes of different widths [138, 139]. To analyze the data, the edge force model of Hu [143] was used. This model describes the effect of the  $\text{Si}_3\text{N}_4$  film on the substrate by a force  $f$  parallel to the surface and starting from the edges as shown in Fig. 2.12. It confirms that the stress is uniaxial only in the center of the stripe and that shear stress and stress in the  $\langle 001 \rangle$  direction can not be neglected close to the edges. The Raman shifts calculated with this analytical model are plotted by a straight line and compared to the experimental ones represented in open circles. Despite the simplicity of the model, the results are remarkably good confirming that the model gives a stress distribution close to the real one. There are still small discrepancies. The model predicts larger Raman shifts than observed at the edges. It might come



from a small defocusing of the laser spot or to an overestimation of the stress given by the model. As the stripe width decreases, the relaxation of the compressive stress in the center of the stripe decreases and vanishes for the  $2.1\text{ }\mu\text{m}$  stripe. This is only due to the limitation coming from the spatial resolution. Since the  $457.9\text{ nm}$  line of the Ar laser is focused to a spot of around  $1\text{ }\mu\text{m}$  and penetrates up to  $300\text{ nm}$  deep into silicon, the stress measured is a weighted average over the penetration depth and the laser spot size. Moreover, the analytical model fails for this narrow stripe and gives an unexpected shoulder at the edges. This small discrepancy emphasizes the pitfall to univocally correlate the stress tensor to the experimental strain-induced Raman shifts. Some answers will be given in the next section to fix partially this issue.

### ***2.3.2 Stress Mapping of Shallow Trench Isolation***

Scaling down LOCOS to smaller dimensions is mainly limited by the lateral encroachment of the FOX under the nitride mask that reduces the active area dimensions as compared to the dimensions of the nitride mask. Moreover, if the bird's peak length is larger than half the nitride length, the bird's peak originating from both sides of the nitride will overlap and a thick oxide will be grown underneath the nitride. This phenomenon is known as bird's peak punch through or nitride lifting. If the pad oxide thickness increases significantly owing to this phenomenon, it will be impossible to remove it during the removal of the oxidation mask, and the active region will remain covered with an oxide layer, thus preventing the fabrication of devices. This is why LOCOS isolation techniques are no longer adequate for sub- $0.25\text{ }\mu\text{m}$  integrated circuit processing [32] and has to be replaced by STI. The process sequence is very similar. The active areas are defined in the same way with the combination of a pad oxide and a  $\text{Si}_3\text{N}_4$  film on top. The isolation trenches are etched by reactive ion etching (RIE). Then a thermal oxide is grown at high temperature on the trench walls. The process conditions of this step must be optimized to getter the defects induced by RIE and to smoothen the edges of the trenches. Finally, several oxidation and oxide deposition processes are combined to fill the trenches and minimize the stress induced by such high temperature steps.

The most important benefit of STI is that it allows an independent control of the isolation depth with respect to the isolation width. The width is primarily defined by lithography, while the isolation depth is solely controlled by the trench etch. STI reduces also the final topography induced by the LOCOS process. Because of the nature of silicon oxidation, about 50 % or greater of the oxide thickness is above the silicon surface. This topography is especially problematic for optical lithography with limited depth of focus. Despite these advantages, STI is one of the most critical technology modules from the point of view of defect generation during the process. The defect generation is directly related to the mechanical stress surrounding the trench. This is why the effect of processing conditions and trench geometry on the stress magnitude has been extensively studied in the literature [134, 135, 144–151].



Since the switch from LOCOS to STI is driven by the shrinking of the pattern size, the weighted average over the penetration depth and the laser spot size becomes even more detrimental to study the stress induced by such small structures. The first answer is then to perform Raman imaging with a smaller wavelength to decrease both the penetration depth and the laser spot size. In this way, Dombrowski et al. [144, 146] studied the evolution of the stress in STI stripes of different widths during their fabrication. They evidenced the benefits of using UV laser (363.8 nm) compared to visible laser (457.9 nm). The main advantage was to decrease the penetration depth from 300 nm down to 10 nm. This smaller penetration depth enabled to detect a very large stress that was confined in the vicinity of the surface. The spatial resolution was also improved, the spot size decreasing from 1 down to 0.7  $\mu\text{m}$ . With such experimental improvements, Dombrowski et al. identified a critical process step which increases strongly the compressive stress at the edges. After the sidewall oxidation, if a wet oxidation process is used instead of a dry oxidation, it results in an increased sidewall oxide thickness and in the formation of a large bird's peak under the nitride. This observation was confirmed by scanning electron microscopy (SEM) experiments. Although the stress was qualitatively estimated from the usual uniaxial assumption, this example is an excellent demonstration that Raman imaging is a powerful tool for process monitoring. It can identify easily and nondestructively a potentially dangerous process step. Moreover, it avoided to perform tedious TEM experiments to identify this issue.

According to Poborchii et al. [150, 152, 153], using oil-immersion objective lenses with the 363.8 nm wavelength improves the spatial resolution down to 150 nm. Thanks to this improvement, they performed Raman mapping of the STI structures sketched in Fig. 2.13. These structures were composed of Si stripes surrounded by  $\text{SiO}_2$  trenches. The Si stripes were oriented along the  $\langle 1-10 \rangle$  axis and were 250 nm wide. The oxide trenches were 300 nm deep and 1  $\mu\text{m}$  wide. For this study, a specific system of axes was defined. It is represented in Fig. 2.13, where  $a$ ,  $b$  and  $c$  are, respectively, parallel to the  $\langle 110 \rangle$ ,  $\langle 001 \rangle$  and  $\langle 1-10 \rangle$  crystalline directions. These structures were measured in the backscattering geometry with two different laser incidences. The first was realized in the standard configuration, the laser being aligned along the  $b$  axis [153]. The second was performed on the cross-section of the STI (on the cleaved edge of the sample) [150]. The laser was in this case aligned along the  $c$  axis. Combining different polarizations of the incident and scattered light enables to measure five different Raman modes:  $aa$ ,  $ca$ ,  $cc$  from the standard backscattering geometry;  $aa$ , and  $ab$  from the backscattering on the cross-section. The first letter stands for the direction of the incident polarization and the second for the direction of the scattered one. Notice that the  $ca$  Raman mode is forbidden by the selection rules for the three stress examples described before. This means that the shear strains  $\varepsilon_{xz}$  and  $\varepsilon_{yz}$  must be different from zero to explain the observation of this mode. Moreover, it is very intense at the edges of the stripes and vanishes outside. This was confirmed by finite element stress simulations [149, 154] which show that, in addition to the  $\langle 110 \rangle$  stress, contributions of the  $\langle 001 \rangle$  stress and shear stress become important in the edge area.

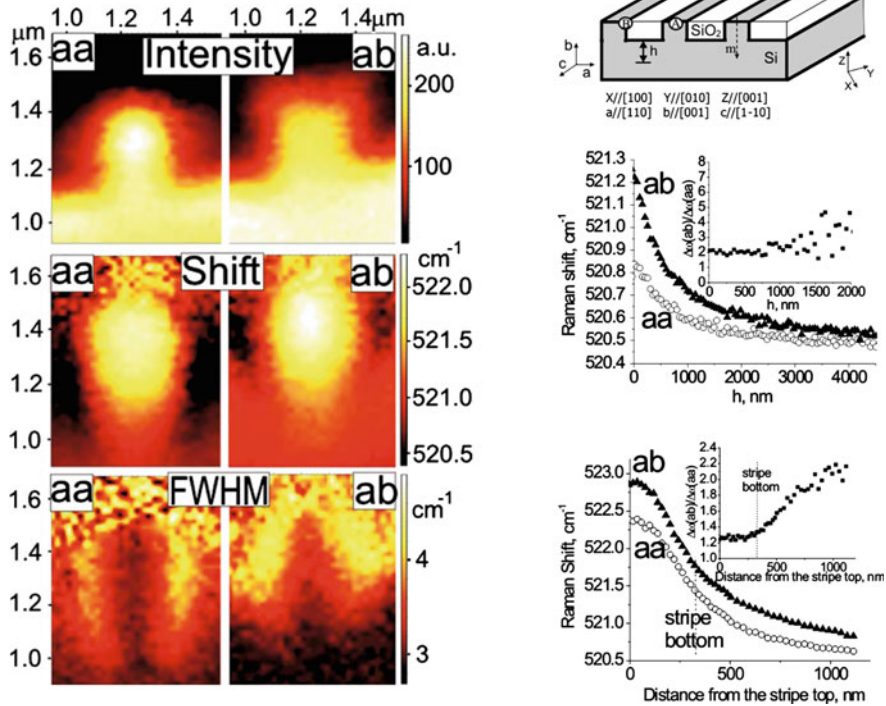


**Fig. 2.13** Raman maps of the cross-section of STI structures sketched in the *top right corner*. Raman spectra were recorded with an oil-immersion objective each 20 nm and fitted by a simple Lorentz curve. Intensities, Raman shifts, and broadening were evaluated for two polarization configurations aa and ab. The first letter stands for the direction of the incident polarization and the second for the direction of the scattered one. The 1D profiles shown in the *right-hand side* were extracted from these maps along *h* and *m*. Reprinted with permission from [150]. Copyright 2007, American Institute of Physics

Raman maps in Fig. 2.13 were collected on the cross-section of the STI structures with aa and ab polarization configurations. Spectra were recorded each 20 nm and fitted with a single Lorentz curve. The shape of the stripe given by the intensity maps depends on the polarization configuration. It comes from a stronger Raman scattering at the stripe edges and corners in the ab configuration than in the aa configuration. For both polarizations, a compressive stress is observed in the stripe area, while the bottom corners and parts of the sidewalls experience a tensile stress. Finally, the broadening is the highest at the stripe edges, and on the sidewalls since the stress varies rapidly in these area as it is usually shown by FEM simulations. Poborchii et al. interested themselves to the ratio between the Raman shifts of the aa and ab modes because it gives information about the stress tensor shape and can discriminate between uniaxial stresses aligned along the  $\langle 001 \rangle$  or the  $\langle 110 \rangle$  axes. The stress-induced frequency shifts are indeed given by the following relationships

depending on the uniaxial stress  $\sigma_{110}$  or  $\sigma_{001}$ :

$$\begin{aligned}
 \Delta\omega_{ab} = \Delta\omega_1 &= \frac{(p+q)S_{11} + (p+3q)S_{12} + rS_{44}}{4\omega_0} \sigma_{110} = -2.88\sigma_{110} \\
 \Delta\omega_{aa} = \Delta\omega_3 &= \frac{qS_{11} + (p+q)S_{12}}{2\omega_0} \sigma_{110} = -2.3\sigma_{110} \\
 \Delta\omega_{ab} = \Delta\omega_{x,y} &= \frac{qS_{11} + (p+q)S_{12}}{2\omega_0} \sigma_{001} = -2.3\sigma_{001} \\
 \Delta\omega_{aa} = \Delta\omega_z &= \frac{pS_{11} + 2qS_{12}}{2\omega_0} \sigma_{001} = -1.13\sigma_{001}
 \end{aligned} \tag{2.30}$$

It means that the ratio  $\Delta\omega_{ab}/\Delta\omega_{aa}$  is equal to 1.25 for  $\langle 110 \rangle$  uniaxial stress and to 2 for  $\langle 001 \rangle$  uniaxial stress. From the FEM simulations, the stress should be  $\langle 110 \rangle$  uniaxial in the middle of the Si stripe just below the surface, and it should be  $\langle 001 \rangle$  uniaxial in the Si substrate beneath the stripes and the trenches. Two profiles were extracted from these maps. The first is along h. It starts from the middle of the trench oxide and goes down in the Si substrate. The ratio  $\Delta\omega_{ab}/\Delta\omega_{aa}$  is constant and equal to 2. This confirms experimentally that the stress is  $\langle 001 \rangle$  uniaxial. It is compressive and equal to  $-310$  MPa near the trench bottom and relaxes completely  $3\text{ }\mu\text{m}$  away in the Si substrate. At  $1\text{ }\mu\text{m}$  it is only equal to  $-90$  MPa. The second profile was extracted along m. It starts from the surface and the middle of the Si stripe. The ratio  $\Delta\omega_{ab}/\Delta\omega_{aa}$  is increasing from 1.25 up to 2. It confirms also that the stress is  $\langle 110 \rangle$  uniaxial in the stripe and gradually transforms into the  $\langle 001 \rangle$  uniaxial stress in the substrate under the stripe bottom. The compressive stress in the middle of the Si stripe was estimated to  $-830$  MPa.

Combining polarized Raman maps from the surface and the cross-section of these STI structures, gives an excellent estimation of the stress fields in such structures that is in good agreement with the FEM simulations [149, 154]. A light  $\langle 001 \rangle$  compression occurs in the substrate just under the oxide trenches. Strong  $\langle 110 \rangle$  compressive stress in the middle of the Si stripe is coupled to weaker tensile stress on the sidewalls and strong shear stress around the top and bottom corners. Finally, a strong Raman intensity enhancement was observed if the incident polarization is aligned along the  $c$  axis (i.e. the stripe length) [151, 152]. This enhancement results from a high confinement of the electromagnetic field at the top corners of the Si stripes. Finite difference time domain (FDTD) simulation reveals that the light is localized in a very small area ( $<20\text{ nm}$ ) around the edge [152]. This light confinement increases with the real part of the dielectric constant of silicon. This effect is therefore quite strong for near UV experiments, while it is very weak for visible light. Enhancement factor of 100 times has been experimentally demonstrated by measuring Si stripes  $20\text{ nm}$  wide and  $10\text{ nm}$  high [152]. These recent and very promising results push away the main limitation of Raman imaging in microelectronics: the spatial resolution that prevents measuring the stress in the actual FET's channel. This edge-enhanced Raman scattering (EERS) is very similar to the elegant solution to improve spatial resolution detailed in the following chapters: tip enhanced Raman spectroscopy (TERS) which

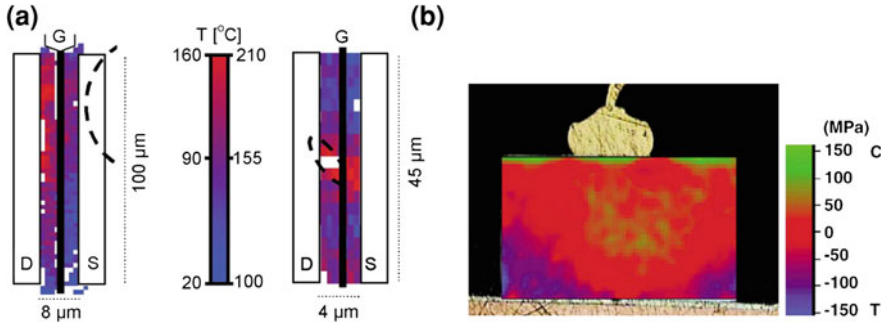


**Fig. 2.14** Temperature maps of two operating AlGaIn/GaN field effect transistors. The local heating comes from the presence of a micropipe underneath the source contact of device (a) and of a microcrack in the channel of device (b). The defects location is marked by the *dashed line*. Reprinted with permission from [160]. Copyright 2007, American Institute of Physics. Stress map of a silicon chip bonded on a Cu substrate. Reprinted from [159]. Copyright 2001, with permission from Elsevier

takes advantage of the huge electric field confinement induced by a sharp metallic tip. Another alternative technique combining Raman spectroscopy with near field techniques: scanning near-field optical Raman microscopy (SNORM) still suffers from a low level of signal and does not significantly improve the spatial resolution compared to oil-immersion objective [155]. To complete this review, stress imaging can also be performed by several interesting techniques such as X-ray micro-diffraction [156], convergent beam electron diffraction [145, 147], and electron holography [157, 158].

## 2.4 Final Device Inspection

Raman imaging contributes to the final device inspection since, both, the performances and reliability are influenced by many unknown parameters during the whole cycle of fabrication. Among them, the presence of temperature or stress fields may cause soft or hard failures during operation. For instance, thermal stress is still a critical reliability issue in ICs packaging and in microelectromechanical systems (MEMS). From  $\mu$ RS the nice point is that it can be easily monitored because the required spatial resolution is on the micron scale or larger.

For instance, Raman imaging has been used to study the stress induced by the anodic bonding of a silicon membrane on a glass substrate, by the thinning, dicing, and packaging of IC [159]. Figure 2.14 shows an illustration of the stress induced by bonding a silicon chip on a Cu substrate. This image was collected on the cross-section and reveals, at the same time, the stress introduced by the solder bump on top of the silicon chip.

Raman imaging can also be used to monitor the temperature in operating devices [26, 160–162]. In this case, several methods are available to calculate the lattice temperature from Raman spectra. The first one consists in measuring the intensity

ratio between the Stokes and anti-Stokes processes as it depends directly on the Bose–Einstein phonon occupation number but, despite its apparent simplicity, this method is time-consuming and prone to systematic errors. For details, see Compaan and Trodhal [163] who reviewed the corrections needed to extract properly the temperature from this ratio in silicon. The other methods rely on the influence of the temperature on the phonons frequencies and lifetimes. Usually, a Raman mode shifts to lower frequencies and broadens with increasing temperature. The broadening arises from the decrease of the phonon lifetime, due to its decay into phonon with lower energies. The downshift of the Raman frequency is mainly due to the effects of thermal expansion and anharmonic coupling to other phonons. The temperature can then be estimated either from the peak shift or from the broadening. However, the peak shift depends both on stress and temperature variations, while the broadening depends only on temperature. This renders possible to measure simultaneously the temperature and stress [162].

In Fig. 2.14, we display two temperature maps collected on AlGaN/GaN field effect transistors. They evidence local self-heating that occurs in the active region of FETs [160]. It is due to a micropipe located underneath the source contact for device (a) and a microcrack in the channel for device (b). These defects are indicated as dashed line in the figure. The presence of such defects reduces locally the thermal conductivity and, therefore, the heat dissipation. Although defects might also influence the current flow in the defect vicinity, these devices had normal DC electrical characteristics and Raman imaging was, in this particular case, of great interest since it could detect such reliability issue.

## 2.5 Conclusion

In this chapter, we have shown that Raman imaging applications cover the whole cycle of fabrication of modern electronic and optoelectronic devices. It enables to check the crystalline quality and the presence of defects during the semiconductor growth, to measure the alloy composition and the doping level. It can also contribute to the final device inspection through temperature mapping of the operating devices. However, its main application is to monitor and control the stress introduced by the different steps in the process flow chart.

## References

1. C.V. Raman, A new class of spectra due to secondary radiation. *Indian J. Phys.* **2**, 387–400 (1928)
2. C.V. Raman, A change of wave-length in light scattering. *Nature* **121**, 619 (1928)
3. P.Y. Yu, M. Cardona, *Fundamentals of Semiconductors: Physics and Materials Properties*, 3rd edn. (Springer, Berlin, 2005)

4. W.H. Weber, R. Merlin (eds.), *Raman Scattering in Materials Science*, Springer Series in Materials Science, vol. 42 (Springer, Berlin, 2000)
5. S. Nakashima, Raman imaging of semiconductor materials: characterization of static and dynamic properties. *J. Phys. Condens. Matter* **16**(2), S25–S37 (2004)
6. G. Gouadec, P. Colombari, Raman spectroscopy of nanomaterials: how spectra relate to disorder, particle size and mechanical properties. *Prog. Cryst. Growth Charact. Mater.* **53**(1), 1–56 (2007)
7. R. Zheng, M. Matsuura, Electron-phonon interaction in mixed crystals. *Phys. Rev. B* **59**(23), 15422–15429 (1999)
8. P.N. Keating, Effect of invariance requirements on the elastic strain energy of crystals with application to the diamond structure. *Phys. Rev.* **145**, 637–645 (1966)
9. H. Rücker, M. Methfessel, Anharmonic Keating model for group-IV semiconductors with application to the lattice dynamics in alloys of Si, Ge, and C. *Phys. Rev. B* **52**, 11059–11072 (1995)
10. J. Menendez, P. Gopalan, G.S. Spencer, N. Cave, J.W. Strane, Raman-spectroscopy study of microscopic strain in epitaxial  $\text{Si}_{1-x-y}\text{Ge}_x\text{C}_y$  alloys. *Appl. Phys. Lett.* **66**(10), 1160–1162 (1995)
11. H. Okumura, E. Sakuma, J.H. Lee, H. Mukaida, S. Misawa, K. Endo, S. Yoshida, Raman scattering of SiC: Application to the identification of heteroepitaxy of SiC polytypes. *J. Appl. Phys.* **61**(3), 1134–1136 (1987)
12. J. Camassel, S. Contreras, J.L. Robert, SiC materials: a semiconductor family for the next century. *Compte. Rendu. de l'Acad. des Sci. Paris* **1**(Série IV), p5–p21 (2000)
13. K. Zekentes, K. Rogdakis, SiC nanowires: material and devices. *J. Phys. D Appl. Phys.* **44**(13), 133001 (2011)
14. P.J. Wellmann, T. Straubinger, U. Kunecke, R. Muller, S.A. Sakwe, M. Pons, A. Thuaiere, A. Crisci, M. Mermoux, L. Auvray, J. Camassel, Optical mapping of aluminum doped p-type SiC wafers. *Phys. Status Solidi A* **202**(4), 598–601 (2005)
15. J.C. Burton, L. Sun, M. Pophristic, S.J. Lukacs, F.H. Long, Z.C. Feng, I.T. Ferguson, Spatial characterization of doped SiC wafers by Raman spectroscopy. *J. Appl. Phys.* **84**(11), 6268–6273 (1998)
16. H. Harima, S.-I. Nakashima, T. Uemura, Raman scattering from anisotropic LO-phonon-plasmon-coupled mode in n-type 4H- and 6H-SiC. *J. Appl. Phys.* **78**(3), 1996–2005 (1995)
17. P. Perlin, J. Camassel, W. Knap, T. Taliercio, J.C. Chervin, T. Suski, I. Grzegory, S. Porowski, Investigation of longitudinal-optical phonon-plasmon coupled modes in highly conducting bulk GaN. *Appl. Phys. Lett.* **67**(17), 2524–2526 (1995)
18. S. Ganesan, A.A. Maradudin, J. Oitmaa, A lattice theory of morphic effects in crystals of the diamond structure. *Ann. Phys.* **56**(2), 556–594 (1970)
19. M.H. Grimsditch, E. Anastassakis, M. Cardona, Effect of uniaxial stress on the zone-center optical phonon of diamond. *Phys. Rev. B* **18**(2), 901–904 (1978)
20. B. Dietrich, V. Bukalo, A. Fischer, K.F. Dombrowski, E. Bugiel, B. Kuck, H.H. Richter, Raman-spectroscopic determination of inhomogeneous stress in submicron silicon devices. *Appl. Phys. Lett.* **82**(8), 1176–1178 (2003)
21. A. Steegen, I. De Wolf, K. Maex, Characterization of the local mechanical stress induced during the Ti and Co/Ti salicidation in sub-0.25  $\mu\text{m}$  technologies. *J. Appl. Phys.* **86**(8), 4290–4297 (1999)
22. K. Pinardi, S.C. Jain, M. Willander, A. Atkinson, H.E. Maes, R. Van Overstraeten, A method to interpret micro-Raman experiments made to measure nonuniform stresses: application to local oxidation of silicon structures. *J. Appl. Phys.* **84**(5), 2507–2512 (1998)
23. M. Bowden, D.J. Gardiner, D. Wood, J. Burdess, A. Harris, J. Hedley, Raman and finite-element analysis of a mechanically strained silicon microstructure. *J. Micromech. Microeng.* **11**(1), 7–12 (2001)
24. E. Anastassakis, A. Cantarero, M. Cardona, Piezo-Raman measurements and anharmonic parameters in silicon and diamond. *Phys. Rev. B* **41**(11), 7529–7535 (1990)



25. M. Mermoux, B. Marcus, A. Crisci, A. Tajani, E. Gheeraert, E. Bustarret, Micro-Raman scattering from undoped and phosphorous-doped (111) homoepitaxial diamond films: stress imaging of cracks. *J. Appl. Phys.* **97**(4), 043530 (2005)
26. X.D. Pu, J. Chen, W.Z. Shen, H. Ogawa, Q.X. Guo, Temperature dependence of Raman scattering in hexagonal indium nitride films. *J. Appl. Phys.* **98**(3), 033527 (2005)
27. N. Camara, A. Tiberj, B. Jouault, A. Caboni, B. Jabakhanji, N. Mestres, P. Godignon, J. Camassel, Current status of self-organized epitaxial graphene ribbons on the C face of 6H-SiC substrates. *J. Phys. D Appl. Phys.* **43**(37), 374011 (2010)
28. O. Martinez, L.F. Sanz, J. Jimenez, A. Martin-Martin, B. Gerard, E. Gil-Lafon, Stress distribution mapping of GaAs on Si conformal layers. *J. Appl. Phys.* **101**(5), 054901 (2007)
29. C.-H. Chen, C.-M. Yeh, J. Hwang, T.-L. Tsai, C.-H. Chiang, C.-S. Chang, T.-P. Chen, Band gap shift in the GaN/AlN multilayers on the mesh-patterned Si(111). *Appl. Phys. Lett.* **88**(16), 161912 (2006)
30. C.-H. Chen, C.-M. Yeh, J. Hwang, T.-L. Tsai, C.-H. Chiang, C.-S. Chang, T.-P. Chen, Stress relaxation in the GaN/AlN multilayers grown on a mesh-patterned Si(111) substrate. *J. Appl. Phys.* **98**(9), 093509 (2005)
31. S. Nakashima, H. Harima, N. Ohtani, M. Katsuno, Raman characterization of local electrical properties and growth process in modulation-doped 6H-SiC crystals. *J. Appl. Phys.* **95**(7), 3547–3552 (2004)
32. The Latest International Technology Roadmap for Semi-conductors (ITRS), <http://www.public.itrs.net/>
33. A.H. Castro Neto, F. Guinea, N.M.R. Peres, K.S. Novoselov, A.K. Geim, The electronic properties of graphene. *Rev. Mod. Phys.* **81**(1), 109–162 (Jan 2009)
34. R.R. Nair, P. Blake, A.N. Grigorenko, K.S. Novoselov, T.J. Booth, T. Stauber, N.M.R. Peres, A.K. Geim, Fine structure constant defines visual transparency of graphene. *Science* **320**(5881), 1308 (2008)
35. N. Ferralis, Probing mechanical properties of graphene with Raman spectroscopy. *J. Mater. Sci.* **45**(19), 5135–5149 (2010)
36. [http://www.nobelprize.org/nobel\\_prizes/physics/laureates/2010/sci.html](http://www.nobelprize.org/nobel_prizes/physics/laureates/2010/sci.html)
37. A.K. Geim, K.S. Novoselov, The rise of graphene. *Nat. Mater.* **6**(3), 183–191 (2007)
38. P.R. Wallace, *Phys. Rev.* **71**, 476 (1947)
39. K.S. Novoselov, A.K. Geim, S.V. Morozov, D. Jiang, M.I. Katsnelson, I.V. Grigorieva, S.V. Dubonos, A.A. Firsov, Two-dimensional gas of massless dirac fermions in graphene. *Nature* **438**, 197 (2005)
40. Y. Zhang, Y.-W. Tan, H.L. Stormer, P. Kim, Experimental observation of the quantum hall effect and berry's phase in graphene. *Nature* **438**, 201 (2005)
41. K.S. Novoselov, Z. Jiang, Y. Zhang, S.V. Morozov, H.L. Stormer, U. Zeitler, J.C. Maan, G.S. Boebinger, P. Kim, A.K. Geim, Room-temperature quantum Hall effect in graphene. *Science* **315**(5817), 1379 (2007)
42. A. Tzalenchuk, S. Lara-Avila, A. Kalaboukhov, S. Paolillo, M. Syväjärvi, R. Yakimova, O. Kazakova, T.J.B.M. Janssen, V. Fal'ko, S. Kubatkin, Towards a quantum resistance standard based on epitaxial graphene. *Nat. Nanotechnol.* **5**, 186 (2010)
43. L.M. Malard, M.A. Pimenta, G. Dresselhaus, M.S. Dresselhaus, Raman spectroscopy in graphene. *Phys. Rep.* **473**(5–6), 51–87 (2009)
44. G. Eda, G. Fanchini, M. Chhowalla, Large-area ultrathin films of reduced graphene oxide as a transparent and flexible electronic material. *Nat. Nanotechnol.* **3**, 270 (2008)
45. Y. Hernandez, V. Nicolosi, M. Lotya, F.M. Blighe, Z. Sun, S. De I.T. McGovern, B. Holland, M. Byrne, Y.K. Gun'Ko, J.J. Boland, P. Niraj, G. Duesberg, R. Krishnamurthy, R. Goodhue, J. Hutchison, V. Scardaci, A.C. Ferrari, J.N. Coleman, High-yield production of graphene by liquid-phase exfoliation of graphite. *Nat. Nanotechnol.* **3**, 563 (2008)
46. P.W. Sutter, J.-I. Flege, E.A. Sutter, Epitaxial graphene on ruthenium. *Nat. Mater.* **7**(5), 406–411 (2008)
47. I. Pletikosić, M. Kralj, P. Pervan, R. Brako, J. Coraux, A.T. N'diaye, C. Busse, T. Michely, Dirac cones and minigaps for graphene on Ir(111). *Phys. Rev. Lett.* **102**(5), 056808 (2009)

48. J. Coraux, A.T. N'Diaye, C. Busse, T. Michely, Structural coherency of graphene on Ir(111). *Nano Lett.* **8**(2), 565–570 (2008)
49. Y. Lee, S. Bae, H. Jang, S. Jang, S.-E. Zhu, S.H. Sim, Y.I. Song, B.H. Hong, J.-H. Ahn, Wafer-scale synthesis and transfer of graphene films. *Nano Lett.* **10**(2), 490–493 (2010)
50. A. Reina, X. Jia, J. Ho, D. Nezich, H. Son, V. Bulovic, M.S. Dresselhaus, J. Kong, Large area, few-layer graphene films on arbitrary substrates by chemical vapor deposition. *Nano Lett.* **9**(1), 30–35 (2009)
51. K.S. Kim, Y. Zhao, H. Jang, S.Y. Lee, J.M. Kim, K.S. Kim, J.-H. Ahn, P. Kim, J.-Y. Choi, B.H. Hong, Large-scale pattern growth of graphene films for stretchable transparent electrodes. *Nature* **457**(7230), 706–710 (2009)
52. S. Bae, H. Kim, Y. Lee, X. Xu, J.-S. Park, Y. Zheng, J. Balakrishnan, T. Lei, H.R. Kim, Y.I. Song, Y.-J. Kim, K.S. Kim, B. Ozyilmaz, J.-H. Ahn, B.H. Hong, S. Iijima, Roll-to-roll production of 30-inch graphene films for transparent electrodes. *Nat. Nanotechnol.* **5**(8), 574–578 (2010)
53. X. Li, W. Cai, J. An, S. Kim, J. Nah, D. Yang, R. Piner, A. Velamakanni, I. Jung, E. Tutuc, S.K. Banerjee, L. Colombo, R.S. Ruoff, Large-area synthesis of high-quality and uniform graphene films on copper foils. *Science* **324**(5932), 1312–1314 (2009)
54. C. Berger, Z. Song, X. Li, X. Wu, N. Brown, C. Naud, D. Mayou, T. Li, J. Hass, A.N. Marchenkov, E.H. Conrad, P.N. First, W.A. de Heer, Electronic confinement and coherence in patterned epitaxial graphene. *Science* **312**(5777), 1191–1196 (2006)
55. C. Berger, Z.M. Song, T.B. Li, X.B. Li, A.Y. Ogbazghi, R. Feng, Z.T. Dai, A.N. Marchenkov, E.H. Conrad, P.N. First, W.A. de Heer, Ultrathin epitaxial graphite: 2D electron gas properties and a route toward graphene-based nanoelectronics. *J. Phys. Chem. B* **108**(52), 19912–19916 (2004)
56. P. Sutter, Epitaxial graphene: how silicon leaves the scene. *Nat. Mater.* **8**(3), 171–172 (2009)
57. C. Virojanadara, M. Syväjärvi, R. Yakimova, L.I. Johansson, A.A. Zakharov, T. Balasubramanian, Homogeneous large-area graphene layer growth on 6H-SiC(0001). *Phys. Rev. B* **78**(24), 245403 (2008)
58. K.V. Emtsev, A. Bostwick, K. Horn, J. Jobst, G.L. Kellogg, L. Ley, J.L. McChesney, T. Ohta, S.A. Reshanov, J. Roehrl, E. Rotenberg, A.K. Schmid, D. Waldmann, H.B. Weber, T. Seyller, Towards wafer-size graphene layers by atmospheric pressure graphitization of silicon carbide. *Nat. Mater.* **8**(3), 203–207 (2009)
59. S. Kim, J. Ihm, H.J. Choi, Y.-W. Son, Origin of anomalous electronic structures of epitaxial graphene on silicon carbide. *Phys. Rev. Lett.* **100**(17), 176802 (2008)
60. Y. Qi, S.H. Rhim, G.F. Sun, M. Weinert, L. Li, Epitaxial Graphene on SiC(0001): more than just honeycombs. *Phys. Rev. Lett.* **105**(8), 085502 (Aug 2010)
61. F. Varchon, P. Mallet, J.-Y. Veuillen, L. Magaud, Ripples in epitaxial graphene on the Si-terminated SiC(0001) surface. *Phys. Rev. B* **77**(23), 235412 (Jun 2008)
62. H.E. Hoster, M.A. Kulakov, B. Bullemer, Morphology and atomic structure of the SiC(000(1)over-bar) $3 \times 3$  surface reconstruction. *Surf. Sci.* **382**(1–3), L658–L665 (June 1997)
63. F. Hiebel, P. Mallet, F. Varchon, L. Magaud, J.-Y. Veuillen, Graphene-substrate interaction on 6H-SiC(000 $\bar{1}$ ): a scanning tunneling microscopy study. *Phys. Rev. B* **78**(15), 153412 (2008)
64. F. Hiebel, P. Mallet, L. Magaud, J.-Y. Veuillen, Atomic and electronic structure of monolayer graphene on 6H-SiC(000 $\bar{1}$ )( $3 \times 3$ ): a scanning tunneling microscopy study. *Phys. Rev. B* **80**(23), 235429 (2009)
65. N. Camara, J.-R. Huntzinger, G. Rius, A. Tiberj, N. Mestres, F. Pérez-Murano, P. Godignon, J. Camassel, Anisotropic growth of long isolated graphene ribbons on the C face of graphite-capped 6H-SiC. *Phys. Rev. B* **80**(12), 125410 (2009)
66. B. Jouault, B. Jabakhanji, N. Camara, W. Desrat, A. Tiberj, J.-R. Huntzinger, C. Consejo, A. Caboni, P. Godignon, Y. Kopelevich, J. Camassel, Probing the electrical anisotropy of multilayer graphene on the Si face of 6H-SiC. *Phys. Rev. B* **82**(8), 085438 (2010)
67. T. Stauber, N.M.R. Peres, A.K. Geim, Optical conductivity of graphene in the visible region of the spectrum. *Phys. Rev. B* **78**(8), 085432 (2008)



68. A.C. Ferrari, J.C. Meyer, V. Scardaci, C. Casiraghi, M. Lazzeri, F. Mauri, S. Piscanec, D. Jiang, K.S. Novoselov, S. Roth, A.K. Geim, Raman spectrum of graphene and graphene layers. *Phys. Rev. Lett.* **97**(18), 187401 (2006)
69. D.M. Basko, S. Piscanec, A.C. Ferrari, Electron-electron interactions and doping dependence of the two-phonon raman intensity in graphene. *Phys. Rev. B* **80**(16), 165413 (2009)
70. C. Casiraghi, Doping dependence of the raman peaks intensity of graphene close to the dirac point. *Phys. Rev. B* **80**(23), 233407 (2009)
71. L. Patrick, W.J. Choyke, Static dielectric constant of SiC. *Phys. Rev. B* **2**(6), 2255–2256 (1970)
72. A. Das, B. Chakraborty, S. Piscanec, S. Pisana, A.K. Sood, A.C. Ferrari, Phonon renormalization in doped bilayer graphene. *Phys. Rev. B* **79**(15), 155417 (2009)
73. P. Gava, M. Lazzeri, A.M. Saitta, F. Mauri, Probing the electrostatic environment of bilayer graphene using raman spectra. *Phys. Rev. B* **80**(15), 155422 (2009)
74. T. Ando, M. Koshino, Field effects on optical phonons in bilayer graphene. *J. Phys. Soc. Jpn.* **78**(3), 034709 (2009)
75. M. Bruna, S. Borini, Observation of raman g-band splitting in top-doped few-layer graphene. *Phys. Rev. B* **81**(12), 125421 (2010)
76. J. Yan, T. Villarsen, E.A. Henriksen, P. Kim, A. Pinczuk, Optical phonon mixing in bilayer graphene with a broken inversion symmetry. *Phys. Rev. B* **80**(24), 241417 (2009)
77. L.M. Malard, D.C. Elias, E.S. Alves, M.A. Pimenta, Observation of distinct electron-phonon couplings in gated bilayer graphene. *Phys. Rev. Lett.* **101**(25), 257401 (2008)
78. P. Poncharal, A. Ayari, T. Michel, J.-L. Sauvajol, Effect of rotational stacking faults on the raman spectra of folded graphene. *Phys. Rev. B* **79**(19), 195417 (2009)
79. D. Graf, F. Molitor, K. Ensslin, C. Stampfer, A. Jungen, C. Hierold, L. Wirtz, Spatially resolved raman spectroscopy of single- and few-layer graphene. *Nano Lett.* **7**(2), 238–242 (2007)
80. N. Ferralis, Probing mechanical properties of graphene with raman spectroscopy. *J. Mater. Sci.* **45**, 5135–5149 (2010). doi:[10.1007/s10853-010-4673-3](https://doi.org/10.1007/s10853-010-4673-3)
81. T.M.G. Mohiuddin, A. Lombardo, R.R. Nair, A. Bonetti, G. Savini, R. Jalil, N. Bonini, D.M. Basko, C. Galiotis, N. Marzari, K.S. Novoselov, A.K. Geim, A.C. Ferrari, Uniaxial strain in graphene by raman spectroscopy: g peak splitting, gröneisen parameters, and sample orientation. *Phys. Rev. B* **79**(20), 205433 (2009)
82. F. Varchon, R. Feng, J. Hass, X. Li, B. Ngoc Nguyen, C. Naud, P. Mallet, J.-Y. Veuillen, C. Berger, E.H. Conrad, L. Magaud, Electronic structure of epitaxial graphene layers on SiC: effect of the substrate. *Phys. Rev. Lett.* **99**(12), 126805 (2007)
83. J.C. Burton, L. Sun, F.H. Long, Z.C. Feng, I.T. Ferguson, First- and second-order raman scattering from semi-insulating 4H-SiC. *Phys. Rev. B* **59**(11), 7282–7284 (1999)
84. A. Ogura, D. Kosemura, K. Yamasaki, S. Tanaka, Y. Kakemura, A. Kitano, I. Hirokawa, Measurement of in-plane and depth strain profiles in strained-Si substrates. *Solid-State Electron.* **51**(2), 219–225 (2007)
85. D.J. Paul, Si/SiGe heterostructures: from material and physics to devices and circuits. *Semi-cond. Sci. Technol.* **19**(10), R75–R108 (2004)
86. S.-I. Takagi, J.L. Hoyt, J.J. Welser, J.F. Gibbons, Comparative study of phonon-limited mobility of two-dimensional electrons in strained and unstrained Si metal-oxide-semiconductor field-effect transistors. *J. Appl. Phys.* **80**(3), 1567–1577 (1996)
87. R. Oberhuber, G. Zandler, P. Vogl, Subband structure and mobility of two-dimensional holes in strained Si/SiGe MOSFET's. *Phys. Rev. B* **58**(15), 9941–9948 (1998)
88. T. Irisawa, S. Tokumitsu, T. Hattori, K. Nakagawa, S. Koh, Y. Shiraki, Ultrahigh room-temperature hole Hall and effective mobility in  $\text{Si}_{0.3}\text{Ge}_{0.7}/\text{Ge}/\text{Si}_{0.3}\text{Ge}_{0.7}$  heterostructures. *Appl. Phys. Lett.* **81**(5), 847–849 (2002)
89. B. Rössner, D. Chrastina, G. Isella, H. von Känel, Scattering mechanisms in high-mobility strained Ge channels. *Appl. Phys. Lett.* **84**(16), 3058–3060 (2004)
90. C.W. Leitz, M.T. Currie, M.L. Lee, Z.-Y. Cheng, D.A. Antoniadis, E.A. Fitzgerald, Hole mobility enhancements and alloy scattering-limited mobility in tensile strained Si/SiGe surface channel metal-oxide-semiconductor field-effect transistors. *J. Appl. Phys.* **92**(7), 3745–3751 (2002)

91. M.T. Currie, C.W. Leitz, T.A. Langdo, G. Taraschi, E.A. Fitzgerald, D.A. Antoniadis, Carrier mobilities and process stability of strained Si n- and p-MOSFETs on SiGe virtual substrates. *J. Vac. Sci. Technol. B* **19**(6), 2268–2279 (2001)
92. H. Rho, H.E. Jackson, B.L. Weiss, Raman imaging of stress in a SiGe/Si photoelastic optical channel waveguide structure. *Appl. Phys. Lett.* **75**(9), 1287–1289 (1999)
93. S. Nakashima, T. Yamamoto, A. Ogura, K. Uejima, T. Yamamoto, Characterization of Si/Ge<sub>x</sub>Si<sub>1-x</sub> structures by micro-Raman imaging. *Appl. Phys. Lett.* **84**(14), 2533–2535 (2004)
94. M.L. Lee, E.A. Fitzgerald, M.T. Bulsara, M.T. Currie, A. Lochtefeld, Strained Si, SiGe, and Ge channels for high-mobility metal-oxide-semiconductor field-effect transistors. *J. Appl. Phys.* **97**(1), 011101 (2005)
95. J.H. Li, C.S. Peng, Y. Wu, D.Y. Dai, J.M. Zhou, Z.H. Mai, Relaxed Si<sub>0.7</sub>Ge<sub>0.3</sub> layers grown on low-temperature Si buffers with low threading dislocation density. *Appl. Phys. Lett.* **71**(21), 3132–3134 (1997)
96. V. Paillard, P. Puech, R. Sirvin, S. Hamma, P. Roca i Cabarrocas, Measurement of the in-depth stress profile in hydrogenated microcrystalline silicon thin films using Raman spectrometry. *J. Appl. Phys.* **90**(7), 3276–3279 (2001)
97. P. Puech, G. Landa, R. Carles, P.S. Pizani, E. Daran, C. Fontaine, Strain relaxation in [001]- and [111]-GaAs/CaF<sub>2</sub> analyzed by Raman spectroscopy. *J. Appl. Phys.* **77**(3), 1126–1132 (1995)
98. P.S. Pizani, C.E.M. Campos, Raman probing of thermal damage depth profile in annealed GaAs. *J. Appl. Phys.* **84**(12), 6588–6591 (1998)
99. M.J. Matthews, J.W.P. Hsu, S. Gu, T.F. Kuech, Carrier density imaging of lateral epitaxially overgrown GaN using scanning confocal Raman microscopy. *Appl. Phys. Lett.* **79**(19), 3086–3088 (2001)
100. J. Camassel, N. Planes, L. Falkovsky, H. Moller, M. Eickhoff, G. Krotz, SOL thickness dependence of residual strain in SOI material. *Electron. Lett.* **35**(15), 1284–1286 (1999)
101. J. Camassel, L.A. Falkovsky, N. Planes, Strain effect in silicon-on-insulator materials: investigation with optical phonons. *Phys. Rev. B* **63**(3), 035309 (2000)
102. A. Tiberj, J. Camassel, N. Planes, Y. Stoemenos, H. Moriceau, O. Rayssac, Effect of silicon nitride and silicon dioxide bonding on the residual stress in layer-transferred SOI, in *Proceedings: Silicon-On-Insulator Technology and Devices XI*, ISBN 1-56677-375-X (Electrochemical Society, Pennington, 2003), p. 117
103. A. Tiberj, B. Fraisse, C. Blanc, S. Contreras, J. Camassel, Evaluation of strain induced by implantation in soi materials. *Phys. Status Solidi (c)* **0**, 1060 (2003)
104. A. Tiberj, B. Fraisse, C. Blanc, S. Contreras, J. Camassel, Process-induced strain in silicon-on-insulator materials. *J. Phys. Condens. Matter* **14**(48), 13411 (2002)
105. J. Camassel, A. Tiberj, Strain effects in device processing of silicon-on-insulator materials. *Appl. Surf. Sci.* **212–213**, 742–748 (2003) (11th International Conference on Solid Films and Surfaces)
106. M. Ichimura, Y. Moriguchi, A. Usami, M. Tabuchi, A. Sasaki, Characterization of GaAs heterolayers by micro-Raman spectroscopy. *J. Cryst. Growth* **149**(3–4), 167–174 (1995)
107. O. Pagés, M.A. Renucci, O. Briot, R.L. Aulombard, Raman study of band bending at ZnSe/GaAs interfaces. *J. Appl. Phys.* **77**(3), 1241–1248 (1995)
108. T. Zhang, M.L. Hsieh, W.R. Branford, M.J. Steer, R.A. Stradling, L.F. Cohen, Observation of bevelled GaSb/InAs quantum wells by Raman mapping. *J. Raman Spectrosc.* **36**(10), 978–983 (2005)
109. R. Srnanek, J. Geurts, M. Lentze, G. Irmer, D. Donoval, P. Brdecka, P. Kordos, A. Förster, B. Sciana, D. Radziejewicz, M. Tlaczala, Study of  $\delta$ -doped GaAs layers by micro-Raman spectroscopy on bevelled samples. *Appl. Surf. Sci.* **230**(1–4), 379–385 (2004)
110. R.M.B. Agaiby, S.H. Olsen, P. Dobrosz, H. Coulson, S.J. Bull, A.G. O'Neill, Nanometer strain profiling through Si/SiGe quantum layers. *J. Appl. Phys.* **104**(1), 013507 (2008)
111. C. Villeneuve, K.K. Bourdelle, V. Paillard, X. Hebras, M. Kennard, Raman spectroscopy study of damage and strain in (001) and (011) Si induced by hydrogen or helium implantation. *J. Appl. Phys.* **102**(9), 094905 (2007)

112. H. Richter, Z.P. Wang, L. Ley, The one phonon Raman spectrum in microcrystalline silicon. *Solid State Commun.* **39**(5), 625–629 (1981)
113. W.-P. Huang, H.H. Cheng, G. Sun, R.-F. Lou, J.H. Yeh, T.-M. Shen, The characteristic of strain relaxation on SiGe virtual substrate with thermal annealing. *Appl. Phys. Lett.* **91**(14), 142102 (2007)
114. J.W.P. Hsu, E.A. Fitzgerald, Y.H. Xie, P.J. Silverman, M.J. Cardillo, Surface morphology of related  $\text{Ge}_x\text{Si}_{1-x}$  films. *Appl. Phys. Lett.* **61**(11), 1293–1295 (1992)
115. J.M. Hartmann, B. Gallas, J. Zhang, J.J. Harris, Gas-source molecular beam epitaxy of SiGe virtual substrates: II. Strain relaxation and surface morphology. *Semicond. Sci. Technol.* **15**(4), 370–377 (2000)
116. S.Y. Shiryayev, F. Jensen, J.W. Petersen, On the nature of cross-hatch patterns on compositionally graded  $\text{Si}_{1-x}\text{Ge}_x$  alloy layers. *Appl. Phys. Lett.* **64**(24), 3305–3307 (1994)
117. T. Spila, P. Desjardins, J. D'Arcy-Gall, R.D. Twesten, J.E. Greene, Effect of steady-state hydrogen coverage on the evolution of crosshatch morphology during  $\text{Si}_{1-x}\text{Ge}_x/\text{Si}(001)$  growth from hydride precursors. *J. Appl. Phys.* **93**(4), 1918–1925 (2003)
118. H. Chen, Y.K. Li, C.S. Peng, H.F. Liu, Y.L. Liu, Q. Huang, J.M. Zhou, Q.-K. Xue, Cross-hatching on a SiGe film grown on a Si(001) substrate studied by Raman mapping and atomic force microscopy. *Phys. Rev. B* **65**(23), 233303 (2002)
119. K. Sawano, S. Koh, Y. Shiraki, N. Usami, K. Nakagawa, In-plane strain fluctuation in strained-Si/SiGe heterostructures. *Appl. Phys. Lett.* **83**(21), 4339–4341 (2003)
120. K. Sawano, N. Usami, K. Arimoto, S. Koh, K. Nakagawa, Y. Shiraki, Observation of strain field fluctuation in SiGe-relaxed buffer layers and its influence on overgrown structures. *Mater. Sci. Semicond. Process.* **8**(1–3), 177–180 (2005)
121. K. Sawano, N. Usami, K. Arimoto, K. Nakagawa, Y. Shiraki, Strain field and related roughness formation in SiGe relaxed buffer layers. *Thin Solid Films* **508**(1–2), 117–119 (2006)
122. K. Sawano, N. Usami, K. Arimoto, K. Nakagawa, Y. Shiraki, Thickness dependence of strain field distribution in SiGe relaxed buffer layers. *Jpn. J. Appl. Phys.* **44**(12), 8445–8447 (2005)
123. B. Ghyselen, J.-M. Hartmann, T. Ernst, C. Aulnette, B. Osternaud, Y. Bogumilowicz, A. Abbadie, P. Besson, O. Rayssac, A. Tiberj, N. Daval, I. Cayrefourcq, F. Fournel, H. Moriceau, C. Di Nardo, F. Andrieu, V. Paillard, M. Cabié, L. Vincent, E. Snoeck, F. Cristiano, A. Rocher, A. Ponchet, A. Claverie, P. Boucaud, M.-N. Semeria, D. Bensahel, N. Kernevez, C. Mazure, Engineering strained silicon on insulator wafers with the Smart Cut<sup>TM</sup> technology. *Solid-State Electron.* **48**(8), 1285–1296 (2004)
124. A. Tiberj, V. Paillard, C. Aulnette, N. Daval, K.K. Bourdelle, M. Moreau, M. Kennard, I. Cayrefourcq, Stress metrology: the challenge for the next generation of engineered wafers, in *High-Mobility Group-IV Materials and Devices, Proceedings of MRS Symposium*, vol. 809, San Francisco, pp. 97–102, 2004
125. J.C. Tsang, P.M. Mooney, F. Dacol, J.O. Chu, Measurements of alloy composition and strain in thin  $\text{Ge}_x\text{Si}_{1-x}$  layers. *J. Appl. Phys.* **75**(12), 8098–8108 (1994)
126. F. Pezzoli, E. Bonera, E. Grilli, M. Guzzi, S. Sanguinetti, D. Chrastina, G. Isella, H. von Känel, E. Wintersberger, J. Stangl, G. Bauer, Phonon strain shift coefficients in  $\text{Si}_{1-x}\text{Ge}_x$  alloys. *J. Appl. Phys.* **103**(9), 093521 (2008)
127. J. Groenen, R. Carles, S. Christiansen, M. Albrecht, W. Dorsch, H.P. Strunk, H. Wawra, G. Wagner, Phonons as probes in self-organized SiGe islands. *Appl. Phys. Lett.* **71**(26), 3856–3858 (1997)
128. H.K. Shin, D.J. Lockwood, J.-M. Baribeau, Strain in coherent-wave SiGe/Si superlattices. *Solid State Commun.* **114**(10), 505–510 (2000)
129. S.H. Olsen, A.G. O'Neill, D.J. Norris, A.G. Cullis, N.J. Woods, J. Zhang, K. Fobelets, H.A. Kemhadjian, Strained Si/SiGe n-channel MOSFETs: impact of cross-hatching on device performance. *Semicond. Sci. Technol.* **17**(7), 655–661 (2002)
130. N. Sugii, Thermal stability of the strained-Si/ $\text{Si}_{0.7}\text{Ge}_{0.3}$  heterostructure. *J. Appl. Phys.* **89**(11), 6459–6463 (2001)
131. A. Ogura, K. Yamasaki, D. Kosemura, S. Tanaka, I. Chiba, R. Shimidzu, UV-Raman spectroscopy system for local and global strain measurements in Si. *Jpn. J. Appl. Phys.* **45**(4B), 3007–3011 (2006)

132. J.B. Renucci, R.N. Tyte, M. Cardona, Resonant Raman scattering in silicon. *Phys. Rev. B* **11**(10), 3885–3895 (1975)
133. K. Sawano, Y. Ozawa, A. Fukumoto, N. Usami, J. Yamanaka, K. Suzuki, K. Arimoto, K. Nakagawa, Y. Shiraki, Strain-field evaluation of strain-relaxed thin SiGe layers fabricated by ion implantation method. *Jpn. J. Appl. Phys.* **44**(43), L1316–L1319 (2005)
134. I. De Wolf, Stress measurements in Si microelectronics devices using Raman spectroscopy. *J. Raman Spectrosc.* **30**(10), 877 (1999)
135. I. De Wolf, Micro-Raman spectroscopy to study local mechanical stress in silicon integrated circuits. *Semicond. Sci. Technol.* **11**(2), 139–154 (1996)
136. S.M. Hu, Stress-related problems in silicon technology. *J. Appl. Phys.* **70**(6), R53–R80 (1991)
137. K. Mistry, C. Allen, C. Auth, B. Beattie, D. Bergstrom, M. Bost, M. Brazier, M. Buehler, A. Cappellani, R. Chau, C.-H. Choi, G. Ding, K. Fischer, T. Ghani, R. Grover, W. Han, D. Hanken, M. Hattendorf, J. He, J. Hicks, R. Huessner, D. Ingerly, P. Jain, R. James, L. Jong, S. Joshi, C. Kenyon, K. Kuhn, K. Lee, H. Liu, J. Maiz, B. McIntyre, P. Moon, J. Neiryneck, S. Pei, C. Parker, D. Parsons, C. Prasad, L. Pipes, M. Prince, P. Ranade, T. Reynolds, J. Sandford, L. Schifren, J. Sebastian, J. Seiple, D. Simon, S. Sivakumar, P. Smith, C. Thomas, T. Troeger, P. Vandervoorn, S. Williams, K. Zawadzki, A 45 nm logic technology with high-k plus metal gate transistors, strained silicon, 9 Cu interconnect layers, 193 nm dry patterning, and 100% Pb-free packaging, in *2007 IEEE International Electron Devices Meeting*, vols. 1–2, pp. 247–250, 2007
138. I. De Wolf, E. Anastassakis, Addendum: “Stress measurements in silicon devices through Raman spectroscopy: bridging the gap between theory and experiment” [*J. Appl. Phys.* **79**, 7148 (1996)]. *J. Appl. Phys.* **85**(10), 7484–7485 (1999)
139. I. De Wolf, H.E. Maes, S.K. Jones, Stress measurements in silicon devices through Raman spectroscopy: bridging the gap between theory and experiment. *J. Appl. Phys.* **79**(9), 7148–7156 (1996)
140. I. De Wolf, J. Vanhellemont, A. Romano-Rodríguez, H. Norström, H.E. Maes, Micro-Raman study of stress distribution in local isolation structures and correlation with transmission electron microscopy. *J. Appl. Phys.* **71**(2), 898–906 (1992)
141. I. De Wolf, H. Norström, H.E. Maes, Process-induced mechanical stress in isolation structures studied by micro-Raman spectroscopy. *J. Appl. Phys.* **74**(7), 4490–4500 (1993)
142. S.C. Jain, A.H. Harker, A. Atkinson, K. Pinardi, Edge-induced stress and strain in stripe films and substrates: a two-dimensional finite element calculation. *J. Appl. Phys.* **78**(3), 1630–1637 (1995)
143. S.M. Hu, Film-edge-induced stress in substrates. *J. Appl. Phys.* **50**(7), 4661–4666 (1979)
144. K.F. Dombrowski, B. Dietrich, I. De Wolf, R. Rooyackers, G. Badenes, Investigation of stress in shallow trench isolation using UV micro-Raman spectroscopy. *Microelectron. Reliab.* **41**(4), 511–515 (2001)
145. V. Senez, A. Armigliato, I. De Wolf, G. Carnevale, R. Balboni, S. Frabboni, A. Benedetti, Strain determination in silicon microstructures by combined convergent beam electron diffraction, process simulation, and micro-Raman spectroscopy. *J. Appl. Phys.* **94**(9), 5574–5583 (2003)
146. K.F. Dombrowski, I. De Wolf, B. Dietrich, Stress measurements using ultraviolet micro-Raman spectroscopy. *Appl. Phys. Lett.* **75**(16), 2450–2451 (1999)
147. I. De Wolf, V. Senez, R. Balboni, A. Armigliato, S. Frabboni, A. Cedola, S. Lagomarsino, Techniques for mechanical strain analysis in sub-micrometer structures: TEM/CBED, micro-Raman spectroscopy. X-ray micro-diffraction and modeling. *Microelectron. Eng.* **70**(2–4), 425–435 (2003)
148. R. Liu, M. Canonico, Applications of UV-Raman spectroscopy and high-resolution X-ray diffraction to microelectronic materials and devices. *Microelectron. Eng.* **75**(3), 243–251 (2004)
149. E. Bonera, M. Fanciulli, G. Carnevale, Raman stress maps from finite-element models of silicon structures. *J. Appl. Phys.* **100**(3), 033516 (2006)

150. V. Poborchii, T. Tada, T. Kanayama, Study of stress in a shallow-trench-isolated Si structure using polarized confocal near-UV Raman microscopy of its cross section. *Appl. Phys. Lett.* **91**(24), 241902 (2007)
151. E. Bonera, M. Fanciulli, M. Mariani, Raman spectroscopy of strain in subwavelength micro-electronic devices. *Appl. Phys. Lett.* **87**(11), 111913 (2005)
152. V. Poborchii, T. Tada, T. Kanayama, Edge-enhanced Raman scattering in Si nanostripes. *Appl. Phys. Lett.* **94**(13), 131907 (2009)
153. V. Poborchii, T. Tada, T. Kanayama, High-spatial-resolution Raman microscopy of stress in shallow-trench-isolated Si structures. *Appl. Phys. Lett.* **89**(23), 233505 (2006)
154. S.M. Hu, Stress from isolation trenches in silicon substrates. *J. Appl. Phys.* **67**(2), 1092–1101 (1990)
155. M. Yoshikawa, M. Murakami, K. Matsuda, R. Sugie, H. Ishida, R. Shimizu, Stress characterization of Si by a scanning near-field optical Raman microscope with spatial resolution and with penetration depth at the nanometer level, using resonant Raman scattering. *Jpn. J. Appl. Phys.* **45**(17–19), L486–L489 (2006)
156. C.E. Murray, M. Sankarapandian, S.M. Polvino, I.C. Noyan, B. Lai, Z. Cai, Submicron mapping of strained silicon-on-insulator features induced by shallow-trench-isolation structures. *Appl. Phys. Lett.* **90**(17), 171919 (2007)
157. F. H  , M. H  tch, H. Bender, F. Houdellier, A. Claverie, Direct mapping of strain in a strained silicon transistor by high-resolution electron microscopy. *Phys. Rev. Lett.* **100**(15), 156602 (2008)
158. M. H  tch, F. Houdellier, F. Hue, E. Snoeck, Nanoscale holographic interferometry for strain measurements in electronic devices. *Nature* **453**(7198), 1086–U5 (2008)
159. I. De Wolf, C. Jian, W.M. van Spengen, The investigation of microsystems using Raman spectroscopy. *Opt. Lasers Eng.* **36**(2), 213–223 (2001)
160. J.W. Pomeroy, M. Kuball, D.J. Wallis, A.M. Keir, K.P. Hilton, R.S. Balmer, M.J. Uren, T. Martin, P.J. Heard, Thermal mapping of defects in AlGaIn/GaN heterostructure field-effect transistors using micro-Raman spectroscopy. *Appl. Phys. Lett.* **87**(10), 103508 (2005)
161. T.J. Ochalski, D. Pier  ci  nska, K. Pier  ci  nski, M. Bugajski, J.W. Tomm, T. Grunske, A. Kozłowska, Complementary thermoreflectance and micro-Raman analysis of facet temperatures of diode lasers. *Appl. Phys. Lett.* **89**(7), 071104 (2006)
162. T. Beechem, S. Graham, S.P. Kearney, L.M. Phinney, J.R. Serrano, Invited article: simultaneous mapping of temperature and stress in microdevices using micro-Raman spectroscopy. *Rev. Sci. Instrum.* **78**(6), 061301 (2007)
163. A. Compaan, H.J. Trodahl, Resonance Raman scattering in Si at elevated temperatures. *Phys. Rev. B* **29**(2), 793–801 (1984)



<http://www.springer.com/978-3-642-28251-5>

Raman Imaging  
Techniques and Applications  
Zoubir, A. (Ed.)  
2012, XIV, 386 p., Hardcover  
ISBN: 978-3-642-28251-5